REPORT DOCUMENTATION PAGE

Form Approved
OMB No. 0704-0188

PLEASE DO NOT RETURN YOUR FORM TO THE ABOVE ORGANIZATION.

1. REPORT DATE *(DD-MM-YYYY)*	2. REPORT TYPE	3. DATES COVERED *(From - To)*
11-04-2014	Journal Article	

4. TITLE AND SUBTITLE

Remote sensing of selected water-quality indicators with the hyperspectral imager for the coastal ocean (HICO) sensor

5a. CONTRACT NUMBER

5b. GRANT NUMBER

5c. PROGRAM ELEMENT NUMBER

0602435N

6. AUTHOR(S)

Darryl J. Keitha, Blake A. Schaeffer, Ross S. Lunetta, Richard W. Gould Jr., Kenneth Rocha, and Donald J. Cobb

5d. PROJECT NUMBER

5e. TASK NUMBER

5f. WORK UNIT NUMBER

73-9350-01-5

7. PERFORMING ORGANIZATION NAME(S) AND ADDRESS(ES)

Naval Research Laboratory
Oceanography Division
Stennis Space Center, MS 39529-5004

8. PERFORMING ORGANIZATION REPORT NUMBER

NRL/JA/7330--13-1941

9. SPONSORING/MONITORING AGENCY NAME(S) AND ADDRESS(ES)

Office of Naval Research
One Liberty Center
875 North Randolph Street, Suite 1425
Arlington, VA 22203-1995

10. SPONSOR/MONITOR'S ACRONYM(S)

ONR

11. SPONSOR/MONITOR'S REPORT NUMBER(S)

12. DISTRIBUTION/AVAILABILITY STATEMENT

Approved for public release, distribution is unlimited.

13. SUPPLEMENTARY NOTES

14. ABSTRACT

The Hyperspectral Imager for the Coastal Ocean (HICO) offers the coastal environmental monitoring community an unprecedented opportunity to observe changes in coastal and estuarine water quality across a range of spatial scales not feasible with traditional field-based monitoring or existing ocean colour satellites. HICO, an Office of Naval Research-sponsored programme, is the first space-based maritime hyperspectral imaging instrument designed specifically for the coastal ocean. HICO has been operating since September 2009 from the Japanese Experiment Module - Exposed Facility on the International Space Station (ISS). The high pixel resolution (approximately 95 m at nadir) and hyperspectral imaging capability offer a unique opportunity for characterizing a wide range of water colour constituents that could be used to assess environmental condition. In this study, we transform atmospherically corrected ISS/HICO hyperspectral imagery and derive environmental response variables routinely used for evaluating the environmental condition of coastal ecosystem resources. Using atmospherically corrected HICO imagery and a comprehensive field validation programme, three regionally specific algorithms were developed to estimate basic water-quality properties traditionally measured by monitoring agencies. Results indicated that a three-band chlorophyll a algorithm performed best ($R2 = 0.62$) when compared with in situ measurement data collected 2 -4 hours of HICO acquisitions. Coloured dissolved organic matter (CDOM) ($R2 = 0.93$) and turbidity ($R2 = 0.67$) were also highly correlated. The distributions of these water-quality indicators were mapped for four estuaries along the northwest coast of Florida from April 2010 to May 2012.

15. SUBJECT TERMS

remote sensing; HICO sensor

16. SECURITY CLASSIFICATION OF:			17. LIMITATION OF ABSTRACT	18. NUMBER OF PAGES	19a. NAME OF RESPONSIBLE PERSON
a. REPORT	b. ABSTRACT	c. THIS PAGE			Richard Gould
Unclassified	Unclassified	Unclassified	UU	36	19b. TELEPHONE NUMBER *(Include area code)* (228) 688-5587

Reset

Standard Form 298 (Rev. 8/98)
Prescribed by ANSI Std. Z39.18

BLICATION OR PRESENTATION RELEASE REQUEST

13-1231-3168

Pubkey: 8992 NRLINFY 5.0.2

f: (a) NRL Instruction 5600.
(b) NRL Instruction 5510.30D

cl: (1) Two copies of subject paper (or abstract)

( ) Abstract only, published
( ) Book
( ) Conference Proceedings (refereed)
( ) Invited speaker
(X) Journal article (refereed)
( ) Oral Presentation, published
( ) Other, explain

( ) Abstract only, not published
( ) Book chapter
( ) Conference Proceedings (not refereed)
( ) Multimedia report
( ) Journal article (not refereed)
( ) Oral Presentation, not published

STRN NRL/JA/7330-13-1941
Route Sheet No. 7330/
Job Order No. 73-9350-01-5
Classification X U
Sponsor MISC- NONDOD
approval obtained ___ yes X no

e of Paper or Presentation
ter Quality Remote Sensing with the Hyperspectral Imager for the Coastal Ocean (HICO) Sensor

thor(s) Name(s) *(First,MI,Last), Code, Affiliation if not NRL*

Darryl Keith USEPA/Atlantic Ecology Division Blake Schaeffer USEPA/Gulf Ecology Division Ross Lunetta USEPA/Environmental Services Division
Richard W. Gould 7331

s intended to offer this paper to the _____
(Name of Conference)

_____
(Date, Place and Classification of Conference)

nd/or for publication in Int. Journal of Remote Sensing, Unclassified
(Name and Classification of Publication) *(Name of Publisher)*

fter presentation or publication, pertinent publication/presentation data will be entered in the publications data base, in accordance ith reference (a).
is the opinion of the author that the subject paper (is ____) (is not X) classified, in accordance with reference (b).
his paper does not violate any disclosure of trade secrets or suggestions of outside individuals or concerns which have been ommunicated to the Laboratory in confidence. This paper (does ____) (does not X) contain any militarily critical technology.
his subject paper (has ____) (has never X) been incorporated in an official NRL Report.

Richard W. Gould, 7331 — RWGould
Name and Code *(Principal Author)* (Signature)

CODE	SIGNATURE	DATE	COMMENTS
Author(s) Gould	RWGould	9/27/13	Need by 18 Oct 13
			Publicly accessible sources used for this publication
			This is a Final Security Review. Any changes made in the document, after approved by Code 1231, nullify the Security Review.
Section Head N/A			
Branch Head Richard L. Crout, 7330		9/27/2013	
Division Head Ruth H. Preller, 7300		9/27/0	1. Release of this paper is approved. 2. To the best knowledge of this Division, the subject matter of this paper (has ___) (has never X) been classified.
Security, Code 1231		9/30/13	1. Paper or abstract was released. 2. A copy is filed in this office.
Office of Counsel, Code 1008.3	Beede	10/04/2013	Sponsor Approval Attached
ADOR/Director NCST E. R. Franchi, 7000			
Public Affairs *(Unclassified/ Unlimited Only)*, Code 7030.4	Shannon Mensi	10-3-13	30 SEP '13 AM 9:06
Division, Code			
Author, Code			

THIS FORM CANCELS AND SUPERSEDES ALL PREVIOUS VERSIONS

International Journal of Remote Sensing, 2014
Vol. 35, No. 9, 2927–2962, http://dx.doi.org/10.1080/01431161.2014.894663

Remote sensing of selected water-quality indicators with the hyperspectral imager for the coastal ocean (HICO) sensor

Darryl J. Keith[a]*, Blake A. Schaeffer[b], Ross S. Lunetta[c], Richard W. Gould Jr.[d], Kenneth Rocha[a], and Donald J. Cobb[a]

[a]*US EPA National Health and Environmental Effects Research Laboratory, Atlantic Ecology Division, Narragansett, Rhode Island 02882, USA;* [b]*US EPA National Health and Environmental Effects Research Laboratory, Gulf Ecology Division, Gulf Breeze, Florida 32561, USA;* [c]*US EPA National Exposure Research Laboratory, Research Triangle Park, North Carolina 27709, USA;* [d]*Bio-Optical Physical Processes and Remote Sensing Section, Naval Research Laboratory, Stennis Space Center, Mississippi 39529, USA*

(*Received 12 September 2013; accepted 25 January 2014*)

The Hyperspectral Imager for the Coastal Ocean (HICO) offers the coastal environmental monitoring community an unprecedented opportunity to observe changes in coastal and estuarine water quality across a range of spatial scales not feasible with traditional field-based monitoring or existing ocean colour satellites. HICO, an Office of Naval Research-sponsored programme, is the first space-based maritime hyperspectral imaging instrument designed specifically for the coastal ocean. HICO has been operating since September 2009 from the Japanese Experiment Module – Exposed Facility on the International Space Station (ISS). The high pixel resolution (approximately 95 m at nadir) and hyperspectral imaging capability offer a unique opportunity for characterizing a wide range of water colour constituents that could be used to assess environmental condition. In this study, we transform atmospherically corrected ISS/HICO hyperspectral imagery and derive environmental response variables routinely used for evaluating the environmental condition of coastal ecosystem resources. Using atmospherically corrected HICO imagery and a comprehensive field validation programme, three regionally specific algorithms were developed to estimate basic water-quality properties traditionally measured by monitoring agencies. Results indicated that a three-band chlorophyll *a* algorithm performed best (R^2 = 0.62) when compared with *in situ* measurement data collected 2–4 hours of HICO acquisitions. Coloured dissolved organic matter (CDOM) (R^2 = 0.93) and turbidity (R^2 = 0.67) were also highly correlated. The distributions of these water-quality indicators were mapped for four estuaries along the northwest coast of Florida from April 2010 to May 2012. However, before the HICO sensor can be transitioned from proof-of-concept to operational status and its data applied to benefit decisions made by coastal managers, problems with vicarious calibration of the sensor need to be resolved and standardized protocols are required for atmospheric correction. Ideally, the sensor should be placed on a polar orbiting platform for greater spatial and temporal coverage as well as for image synchronization with field validation efforts.

1. Introduction

The Clean Water Act protects waters in the USA (CWA, 1988). The objective of the CWA is to 'restore and maintain the chemical, physical, and biological integrity of the Nation's waters'. This Federal mandate authorizes states, tribes, and US territories, with guidance and oversight from the US Environmental Protection Agency (EPA), to develop and

*Corresponding author. Email: keith.darryl@epa.gov

implement water-quality standards to protect the resources of the Nation's waterways. Water-quality standards include designated uses, defined as the services that a waterbody supports such as drinking water, aquatic life, harvestable species, and recreation. These standards under the CWA are applicable within navigable waters of the USA and extend seaward a distance of three miles from the coast. Therefore, a majority of research by the EPA addresses scientific questions within state waters, estuaries, lakes, rivers, and streams where applicable water-quality regulation could be implemented. Policymakers and environmental managers need tools enabling them to assess the sustainability of watershed ecosystems, and the services they provide, under current and future land-use practices.

Water-quality condition has historically been assessed based on a suite of indicators related directly to the stress of an ecosystem or can serve as an indicator of stress. Examples are concentrations of chlorophyll *a* (Chl *a*), suspended sediment, salinity, coloured dissolved organic matter (CDOM), and temperature. Chl *a* is used as a proxy for phytoplankton biomass and can be an indicator of increased nutrients (Devlin, Bricker, and Painting 2011; Ferreira et al. 2011; Schaeffer et al. 2012) or a direct measure of potential harmful algal bloom development (Stumpf et al. 2003). Suspended sediment concentrations are important for monitoring wind-driven re-suspension events (Chen 2006), a predictive factor for pathogens such as *E. coli* (Nevers and Whitman 2005), and a valuable tracer of anthropogenic disturbance to land (Ricker, Odhiambo, and Church). CDOM serves as a nutrient source and a vector for heavy metals in water (Zhang et al. 2011; Heyes, Miller, and Mason 2004). Detection from space provides a measure of river plume extent and transfer of organic carbon (Tehrani et al. 2013), both critical to the management of coastal aquatic resources.

Measuring this indicator suite often requires field teams to spend hours on boats to collect data from discrete locations, which ultimately will not provide complete information on the spatial and temporal variations of environmental processes in an estuary or a lake. Although this protocol will continue to be necessary for various reasons, water-quality monitoring using remote-sensing technologies may provide the most practical way to ensure that management practices, at temporal and spatial scales relevant to environmental managers and the general public, are achieving sustainability.

Over the last several decades, satellite technology has allowed measurements on a global scale, but often has poor resolution at local scales, which are more relevant to environmental managers and the general public. Remotely sensed water-quality products were first developed for global ocean observations. In 1978, the Coastal Zone Color Scanner (CZCS) began measuring ocean colour parameters such as phytoplankton biomass with a pixel resolution of approximately 1 × 1 km. This satellite lasted until 1982 and served as a proof-of-concept for the Sea-viewing Wide Field of view Sensor (SeaWiFS), which became operational in 1997. This satellite also had a resolution of 1 × 1 km and provided global coverage with daily revisit cycles. In 2002, the Moderate Resolution Imaging Spectroradiometer (MODIS) and the European Space Agency's Medium Resolution Imaging Spectroradiometer (MERIS) became operational with 1 × 1 km resolution providing global coverage. MODIS had daily repeat cycles whereas MERIS had a 1–2 day revisit cycle. MERIS has also collected data at 300 × 300 m pixel resolution whereas MODIS had several bands at 250 and 500 m resolution for use in coastal waters. All three sensors provided important information on the global aspects of water quality. However, the 1 km pixel resolution characteristic of all three sensors and the Case 1 centric algorithms developed from their data have provided limited assessments of near-shore Case 2 coastal waters, estuaries, and lakes. Case 1 waters are defined as those waters in which phytoplankton are the principal constituent responsible for variation in optical properties of the water. Case 2 waters are those waters influenced

not only by phytoplankton but also by other substances (e.g. CDOM, inorganic suspended sediments) (Morel and Prieur 1977; Gordon and Morel 1983).

Because of these limitations, it has been difficult to derive products from these sensors that could be used by environmental managers or researchers to adequately address issues associated with smaller estuaries or those waters in proximity to the land-water continuum. However, there have been some demonstrations of limited success in deriving water-quality products in coastal and inland waters (Ladner et al. 2007; Miller and McKee 2004; Gons, Auer, and Effler 2008; Werdell et al. 2009, Witter et al. 2009).

Owing to the complex interactions between the biotic and abiotic components in estuarine and coastal waters, approaches and methods to develop satellite-based water-quality products are more complicated than in the adjacent open ocean. Currently, there is no single method that can resolve water-quality products across the spatial continuum of lakes, reservoirs, bayous, estuaries, and the near coastal environment at various temporal scales. Furthermore, algorithms traditionally used to derive water-quality products for the global ocean typically fail or fundamentally do not have accurate assumptions when applied to estuarine or coastal waters. Finally, straylight contamination and bottom reflectance typically confound the derivation of products where environmental management needs are greatest along the land–water interface (Schaeffer et al. 2012).

The Hyperspectral Imager for the Coastal Ocean (HICO) on the International Space Station (ISS) is the first space-based, maritime hyperspectral imaging instrument designed specifically to measure water-quality parameters near the land–water interface. HICO is a pushbroom, imaging spectrometer based on the Portable Hyperspectral Imager for Low-Light Spectroscopy (PHILLS) airborne imaging sensor. HICO was developed by the US Naval Research Laboratory (NRL) for the Office of Naval Research (ONR) as an Innovative Naval Prototype (Corson 2011; Corson and Davis 2011). ONR also supported the first three years of operations including the development and operation of the HICO website at Oregon State University (OSU).

HICO offers the environmental monitoring community an unprecedented opportunity to observe changes in coastal and estuarine water quality across a range of spatial scales not feasible with field-based monitoring. The 95 × 95 m (at nadir) spatial and ≤6 nm bandwidth spectral (Lucke et al. 2011) resolution of the HICO instrument offers a unique capability for characterizing a wide range of water colour parameters that can provide a detailed understanding of estuarine and near-coastal environmental conditions.

In this article, we derive and test the robustness of algorithms to derive Chl *a*, CDOM absorption, and turbidity from the spectral signatures of HICO images of four estuarine/coastal systems of northern Florida taken during April 2010–May 2012 on the ISS during ISS Expeditions 24–31.

2. Methods

2.1. Field and laboratory analysis

Field surveys were conducted in four Florida estuaries along the Florida Panhandle during April 2010 and June 2011 to June 2012. The systems selected represented a range of optical characteristics (e.g. high vs. low particulate loads), were of sufficient size to be adequately resolved in remote-sensing imagery, and were close enough to the EPA Gulf Ecology Division (GED) in Gulf Breeze, FL, to make sampling during an ISS overpass feasible. The systems sampled were Pensacola Bay, Choctawhatchee Bay, St Andrews Bay, and St Joseph Bay (Figures 1 and 2). Field sampling and sample analysis were conducted in accordance with an approved Quality Assurance Plan (Schaeffer 2011).

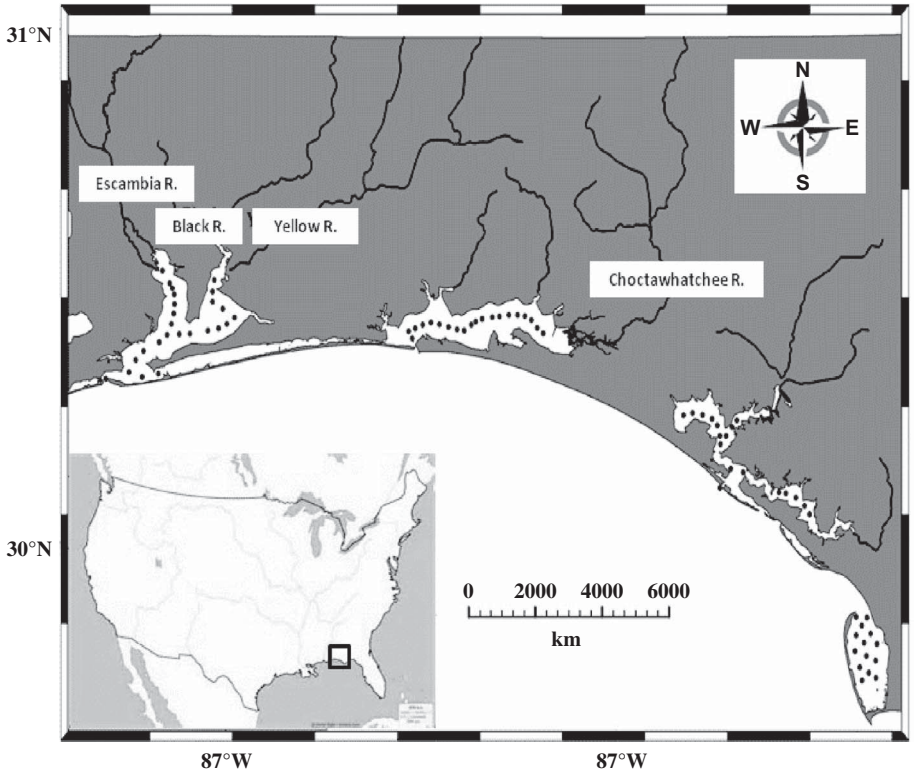

Figure 1. Map of the study region in the northern Gulf of Mexico with only the main rivers identified. Locations of sampling stations are indicated as filled black circles. Estuaries are identified as Pensacola Bay, Choctawhatchee Bay, St Andrews Bay, and St Joseph Bay from left to right.

Three of the coastal systems sampled are characterized as shallow (~4.0 m), microtidal (tidal range ~1.0 m) estuaries located along the northwest Florida coast. Pensacola (30° 42′ N; −87° 22′ W), Choctawhatchee (30° 40′ N; −86° 62′ W), and St Andrews (30° 16′ N; −85° 66′ W) bays are partially mixed, lagoonal estuaries bordered on the ocean side by a barrier island system through which a tidal inlet provides coastal water exchange with the Gulf of Mexico. On the landward side, freshwater discharge is supplied from rivers that drain adjacent watersheds (Figure 1). St Joseph Bay (29° 80′ N; −85° 36′ W) is a slightly deeper (~8 m) coastal embayment partially isolated from the Gulf of Mexico by St Joseph Peninsula and is the only waterbody in the eastern Gulf of Mexico not influenced by the inflow of fresh water (Figure 1).

Sampling stations were located to characterize water quality and optical properties where HICO imagery could be acquired as well as along the major salinity gradients of each estuary (Figure 2). A Sea-Bird 25 CTD (Sea-Bird Electronics, Bellvue, WA, USA) was deployed to measure the vertical profiles of temperature, salinity, and depth. Additional integrated instruments included Chl *a*, turbidity, and CDOM fluorometers. Water samples were collected 0.5 m below the surface, away from boat engines, using a 2L brown Nalgene bottle for the post-cruise analysis of Chl *a* and coloured dissolved organic matter absorption. All collection bottles were triple rinsed with surface water. Samples were typically processed within 24 hours of collection.

Water samples were filtered through Whatman 47 mm GF/F filters (nominal pore size = 0.7 μm) for chlorophyll analysis. Filters were extracted in methanol and

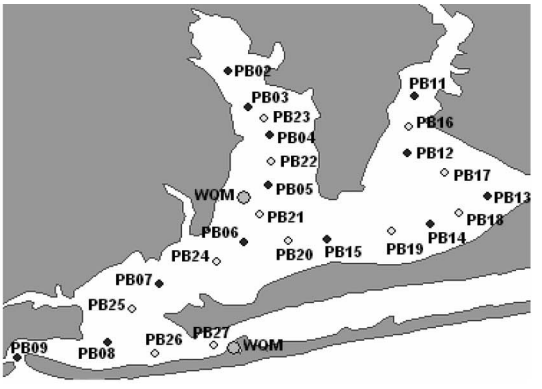

Pensacola Bay

Choctawhatchee Bay

St. Andrew Bay

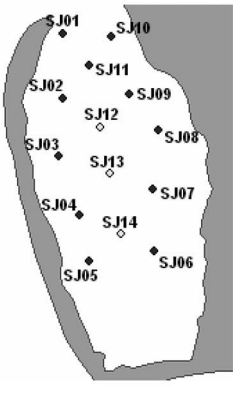

St Joseph Bay

Figure 2. Location of sampling stations within each estuary. Dark circles represent stations where HyperSAS, CTD, and water samples were collected. Open circles represent stations where only HyperSAS and CTD data were collected. In Pensacola Bay, WQM represents the locations of water-quality moorings that provided a time series of chlorophyll, turbidity, and CDOM data.

fluorescence was measured with a Turner Designs (TD700) fluorometer. Associated pigment interference from chlorophyll *b* and phaeopigments were minimized using a 436 nm excitation filter, 680 nm emission filter, and two neutral density reference filters with a blue lamp (Welschmeyer 1994).

CDOM absorption was determined using water filtered through Whatman 47 mm GF/F filters (nominal pore size = 0.7 mm) into combustion glass flasks. Absorption was measured using a 10 cm cuvette with a Shimadzu UV1700 dual-beam spectrophotometer. Data were collected at 1 nm intervals between 200 and 750 nm. Milli-Q deionized water was used in the reference cell. Spectra were normalized by subtracting each wavelength from the measured value at 700 nm (Pegau et al. 2003).

Remote-sensing reflectance (R_{rs}, sr^{-1}) was derived using a hyperspectral surface acquisition system (HyperSAS, Satlantic Inc., Halifax, Nova Scotia). The HyperSAS logged spectral measurements of above-water radiance (Lt(λ)), sky radiance (Li(λ)), and downwelling sky irradiance (Es(λ)) from 350 to 800 nm (interpolated at 1 nm intervals). HyperSAS radiance sensors were mounted on the port side of the pilot house roof of a 25ft boat to provide 40° nadir and zenith viewing angles (Mobley 1999). During data acquisition, the boat was positioned so the radiance sensors were perpendicular to the Sun's azimuth and to avoid boat shadow and wake. The irradiance sensor was mounted above the deck canopy for an unobstructed view of the sky. The above-water remote-sensing reflectance spectra were corrected, following the surface correction algorithm of Gould, Arnone, and Sydor (2001), using the average absorption at 412 nm and the derived spectral scattering shape (Gould, Arnone, and Martinolich 1999). Concurrently with the HyperSAS acquisition, an AC-s (WET-Labs, Philmoth, OR) quantified *in-situ* vertical profiles of absorption (*a*) and beam attenuation (*c*) from 400 to 735 nm interpolated to every 1 nm. Temperature and salinity corrections were applied using corresponding Seabird CTD data (WET-Labs, 2008). The AC-s light absorption (*a*), attenuation (*c*), and derived backscatter (*b*) values were averaged over the surface of the water column to secchi depth.

2.2. *Autonomous underwater vehicles*

Autonomous underwater vehicles (AUVs) were deployed as part of the field programme concurrently with HICO overpasses. The AUVs were operated by the Naval Research Laboratory Stennis Space Center Detachment (NRL/SSC) and the USEPA Atlantic Ecology Division (AED) in Narragansett, Rhode Island.

From August 2011 to May 2012, NRL/SSC deployed a Slocum electric glider five times along the Florida coast. The glider collected *in situ* data roughly following the 15–30 m bathymetric contours just south of the Pensacola Bay. The payload provided profile data of pressure, temperature, conductivity, backscatter (b_b) at 470, 532, and 660 nm, beam attenuation (*c*), chlorophyll fluorescence, and CDOM florescence.

A Hydroid, Konsberg Maritime REMUS 100 (Remote Environmental Monitoring Unit) AUV was acoustically navigated along a predetermined transect via multiple transponder placement. The AUV autonomously surveyed inshore areas using on-board payload sensors, which recorded Chl *a*, turbidity, temperature, conductivity, and salinity data at a depth of approximately one metre. Deployments were designed to coincide with the offshore deployments of the NRL/SSC glider and HICO overpasses. The REMUS 100 was deployed on 19 January 2012 in Escambia Bay, on 20 January 2012 in East Bay sections of greater Pensacola Bay, and on 25 August 2011 and 21 January 2012 in Choctawhatchee Bay.

2.3. *HICO image processing*

During the course of this study, 49 images were acquired from HICO for all four estuaries from April 2010 to May 2012. Images were processed at the EPA AED and an image

from 28 October 2011 was processed by NRL/SSC. The highest number of images (n = 20) was acquired from St Andrews Bay. Sixteen images were acquired from Pensacola Bay, seven images were acquired from Choctawhatchee Bay, and six images were acquired from St Joseph Bay. Each image was part of a scene that covered a 50 × 200 km swath per orbit. Seven images were not processed owing to excessive cloud cover, problems with the Sun's positional data in the header file, or problems warping the image during geo-rectification. The images were acquired between 0800 and 1430 GMT from altitudes ranging from 344 to 421 km above the Earth.

Images from the estuaries were downloaded as radiometrically calibrated Level 1B top-of-atmosphere (TOA) at-sensor radiances from the OSU website (http://hico.coas.oregonstate.edu/index.shtml) (Figure 3, Step 1). The Level 1B data files also contained information that allowed for image geometric correction. The data arrived as a single tar file, which contained 10–12 compressed files associated with each scene including an ASCII header file. Each image is composed of 512 cross-track pixels (samples), 87 bands

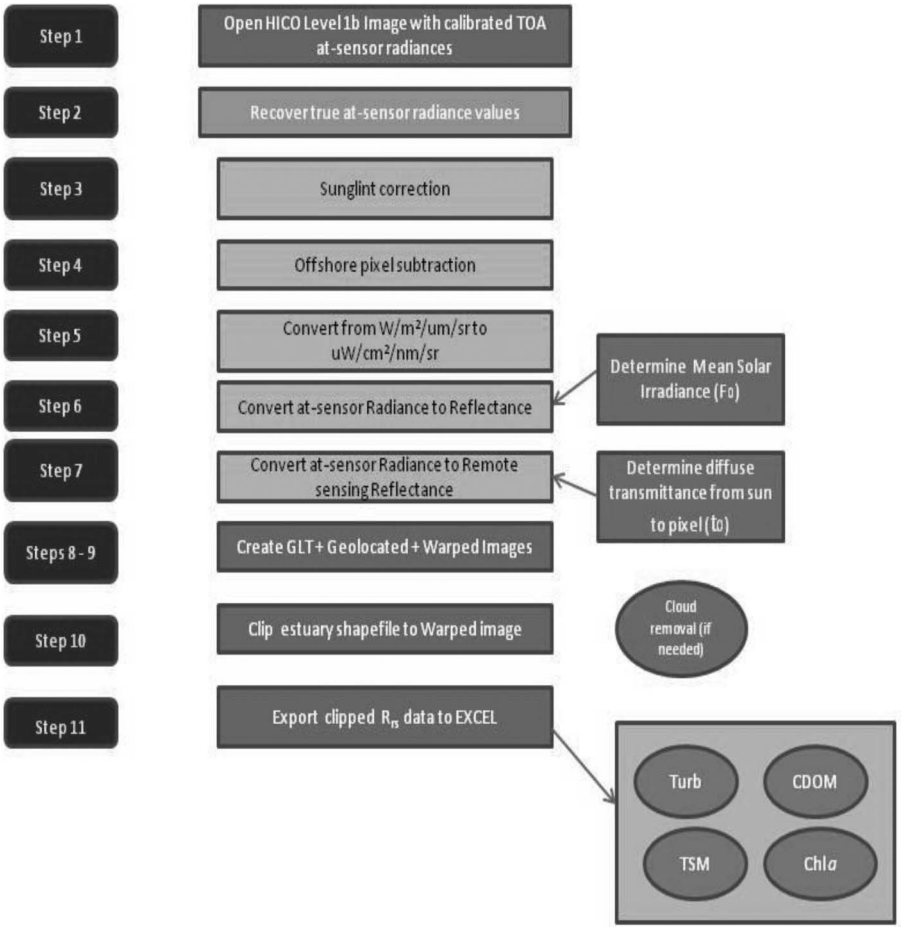

Figure 3. Processing steps used to convert HICO Level 1b radiances to remote-sensing reflectances using the dark-pixel atmospheric correction scheme and export the data for the development of water-quality algorithms.

Table 1. List of acronyms used in equations.

Acronym	Units	Description
λ	nm	Wavelength
Li	W $m^{-2}sr^{-1}\mu m^{-1}$	Wavelength radiance
$L(640)$	W $m^{-2}sr^{-1}\mu m^{-1}$	Radiance at 640 nm
$L(750)$	W $m^{-2}sr^{-1}\mu m^{-1}$	Radiance at 750 nm
$L_t(\lambda)$	W $m^{-2}sr^{-1}\mu m^{-1}$	Total at-sensor radiance
$L_{w\ (offshore)}$	W $m^{-2}sr^{-1}\mu m^{-1}$	Offshore water-leaving radiance
$L_{w\ (estuary)}$	W $m^{-2}sr^{-1}\mu m^{-1}$	Estuary water-leaving radiance
$L_a(\lambda)$	W $m^{-2}sr^{-1}\mu m^{-1}$	Aerosol radiance
$T(\lambda)$		Total transmittance
ρ_w	$_{\mu}$W $m^{-2}sr^{-1}\mu m^{-1}$	Surface reflectance
$L_w(\lambda)$	$_{\mu}$W $m^{-2}sr^{-1}\mu m^{-1}$	Water-leaving radiance
F_0	$_{\mu}$W $m^{-2}sr^{-1}\mu m^{-1}$	Mean solar irradiance
θ_s	degrees	Solar zenith angle
H	km	Altitude
$R_{rs}(\lambda)$	sr^{-1}	Remotely sensed reflectance
t_0		Diffuse transmittance Sun to pixel
τ_r		Rayleigh optical thickness
a_{ph}	m^{-1}	Phytoplankton absorption
a_w	m^{-1}	Water absorption
Chl $a_{\ measured}$	$\mu g\ l^{-1}$	Extracted Chl *a* concentration
Chl $a_{\ predicted}$	$\mu g\ l^{-1}$	Predicted Chl *a* concentration

from 400 to 900 nm, and 2000 lines in ENVI software format and stored as binary files in band sequential (BSQ) format. HICO images were processed using EXELIS ENVI version 4.7. During Step 1, the data were converted to band interleaved format (BIL). A list of acronyms and units used in the following equations is provided in Table 1.

To produce two-byte integer output during pre-Level 1B processing at OSU, the data are multiplied by 50. Therefore, to convert the scaled integer data to geophysical units of $W/m^2/sr/\mu m$, the Level 1B data were divided by 50 (Figure 3, Step 2).

Owing to its low Earth orbit, the ISS is required to make altitude and orbital adjustments due to atmospheric drag, which result in changing solar/viewing geometries of the HICO sensor. These orbital adjustments could result in image pixels getting affected by the specular reflection of light from the sea surface or Sun glint. Sun-glinted pixels are a confounding factor in remote sensing as they may not contain any information about water constituents and benthic features. Pixels affected by Sun glint are common in wide-field-of–view image acquisitions from airborne and satellite missions (Hochberg, Andrefouet, and Tyler 2003). According to Cavalli, Pignatti, and Zappitelli (2006), Sun glint shows strong spatial variations that require individual calculation and correction for each pixel depending on the wave state. During image processing, the method of Goodman, Lee, and Ustin (2008) was used to independently determine the glint radiance for each pixel in a HICO image and correct for Sun glint using the near-infrared (NIR) signal. The major assumptions of this approach are that NIR light is strongly absorbed by water and any signals reflected represent Sun glint reflected from the sea surface. The amount of Sun glint in the NIR band is linearly related to the glint contribution of the visible bands (Hochberg, Andrefouet, and Tyler 2003).

In Step 3, each pixel in a HICO image was corrected to remove the effects of Sun glint by subtracting radiance at 750 nm from the radiance at each wavelength ($L_i(\lambda)$) (Figure 3; Goodman, Lee, and Ustin 2008; Kay, Hedley, and Lavender 2009). An offset was applied

using radiances at 640 ($L(640)$) and 750 ($L(750)$) nm to prevent negative values in the NIR due to over-correction as the corrected radiance approaches zero at 750 nm (Goodman, Lee, and Ustin 2008; Kay, Hedley, and Lavender 2009). The process to correct for Sun glint is expressed as follows:

$$L_i(\lambda) = L_i(\lambda) - L(750) + \Delta, \tag{1}$$

$$\Delta = A + B[L(640) - L(750)], \tag{2}$$

where Δ is the offset, and A + B are the constants. In this approach, we used the values of Goodman et al., which are A = 0.000019 and B = 0.1.

The HICO imagery processed at NRL/SSC was received directly from NRL/DC as level 1B hdf files and processed with the Naval Research Laboratory's Automated Processing System (APS). APS is capable of processing real-time and archived AVHRR, SeaWiFS, MODIS, MERIS, VIIRS, and HICO imagery. It is a powerful, extendable, end-to-end system that includes sensor calibration, atmospheric correction (with NIR correction for coastal waters), and bio-optical inversion (Martinolich and Scardino 2011). APS incorporates, and is consistent with, the latest NASA MODIS code (SeaDAS), which enables production of the NASA standard MODIS products (such as chlorophyll from the OC3 algorithm; O'Reilly et al. 1998), as well as Navy-specific products (such as diver visibility) using NRL algorithms.

2.4. *Atmospheric correction*

The final approach used to atmospherically correct HICO images (Step 4; Figure 3) was determined after an evaluation of results from three processing strategies. During the evaluation, HyperSAS spectral signatures from stations in Pensacola Bay were used as references for comparison (matchups) with spectral outputs derived from the three atmospheric correction approaches. For the NRL/APS processing, the HICO hyperspectral band data were convolved to a reduced band set, representing the MODIS multi-spectral bands, and processed in APS using the standard NASA atmospheric correction (Gordon and Wang 1994) used for MODIS. This approach ensured processing consistency between ocean colour sensors, but did not address sensor inter-calibration issues. Second, HICO images were processed using the ENVI Fast-Line-of-Sight Atmospheric Analysis of Spectral Hypercubes (FLASSH) atmospheric correction programme to retrieve corrected at-surface reflectances (ENVI 2009). FLASSH serves as a user interface to the radiative transfer code MODTRAN 4 (Moderate spectral resolution atmospheric TRANsmittance) (Berk et al. 2000).

Finally, atmospherically corrected at-surface reflectances were retrieved from HICO images using the dark pixel subtraction approach (Themistocleous et al. 2012; Tufillaro, Davis, and Jones 2011; Chavez 1988) to remove atmospheric effects.

The dark pixel approach has been successfully applied to HICO images to retrieve atmospherically corrected radiances from the ocean (e.g. Midway Atoll), coastal (e.g. Columbia River estuary), and near-shore continental shelf (e.g. Clutha and Broadbay, New Zealand) environments by Corson (2010) and Tufillaro, Davis, and Jones (2011). In the dark pixel subtraction approach, atmospheric effects are removed using the at-sensor radiance for a reference pixel characterized by spectra whose radiances were less 'bright' than spectra within the image. These 'darker' radiances are subtracted from the total at-sensor radiances for the image, leaving residual radiances or as in the case for this study

the estuary water-leaving radiances ($L_{w\ (estuary)}$; Figure 5) (Chavez 1988; Goa et al. 2000; Miller and McKee 2004; Wang et al. 2010; Tufillaro, Davis, and Jones 2011).

$$L_T(\lambda) = L_a(\lambda) + T(\lambda)[L_w(\lambda)]. \tag{3}$$

In the dark pixel model of Tufillaro, Davis, and Jones (2011; Equation (3)), $L_T(\lambda)$ is the sensor above-water radiance at a wavelength (λ), L_a accounts for atmospheric and sea-surface reflection, T denotes transmittance from the water surface to sensor, and L_w represents radiances from below the water surface. The contributions to $L_w(\lambda)$ can be decomposed into ($L_d(\lambda)$ + $L_b(\lambda)$), where L_d represents 'clear water' or 'dark pixel' radiances typical for the region and L_b, which represents radiances from 'bright water' within an image.

The premise of the approach begins with imagining, at every pixel, the at-sensor radiance that would be seen if the water was clear (i.e. an idealized spectrum). The difference between the idealized spectrum and the signal observed at-sensor provides information (independent of the atmospheric composition) on the constituents in the water (Tufillaro, Davis, and Jones 2011). Two basic assumptions with this approach were: (1) the atmospheric radiances (L_a) were homogeneous across the scene, such that aerosol size and type did not change over the distance from the dark pixel to the bright pixels, and (2) the amount of light in the red portion of the spectrum emanating from the surface waters of the offshore pixel was negligible. However, previous studies have shown that the second assumption was not entirely valid in coastal areas and may result in an over-correction (Palandro 2006; Themistocleous et al. 2012). We applied a correction procedure to account for this problem (see below, Section 3.1).

The atmospherically corrected radiances that resulted from FLASSH and the dark pixel approach were converted from W $m^{-2}nm^{-1}$ into μW $cm^{-2}nm^{-1}$ (Figure 3; Step 5). In Step 6, the dark pixel corrected L_w values were converted to surface reflectance (ρ_w) following the procedure mentioned in Hu et al. (2004):

$$\rho_w = \frac{(\pi L_w(\lambda))}{F_0 \cos\theta_s}. \tag{4}$$

Remote-sensing reflectance is defined as L_w/E_d. As previously shown, L_w can be derived using the dark pixel approach. However, there is no information on the HICO image header files that allowed for the calculation of E_d. The header file information does allow for the calculation of t_0, F_0, and $\cos\theta_s$. The diffuse transmittance term was derived from Hu et al. (2004):

$$t_0 = \exp\left(\frac{-0.5\,\tau_r}{\cos\theta_s}\right), \tag{5}$$

$$\tau_r = \left(0.0088(\lambda)^{-4.15+0.2\lambda}\right)\left(1 - \exp\left(-0.1188H - 0.011H^2\right)\right), \tag{6}$$

as found in Van Stokkom and Guzzi (1984) and Hansen and Travis (1974).

In Step 7, ρ_w was converted to remote-sensing reflectance $R_{rs}(0+, \lambda)$ sr^{-1} from Hu et al. (2004):

$$R_{rs}(0+,\lambda) = \frac{\rho_w}{(\pi/t_0)}, \quad (7)$$

Because FLASSH retrieved surface reflectances during processing, Step 6 was not applied for conversion of these images. However, FLASSH reflectances were converted to R_{rs} values using Equation (7). In Steps 8 and 9, HICO R_{rs} images were geometrically corrected using information in the rad_geom file associated with each image and projected using geographic (spherical) coordinates (degree units) of longitude and latitude using datum WGS 1984. For this step, the X and Y pixel sizes were initially set to 0.0009° (approximately 100 m; OSU-HICO 2011). In Step 10, the Image-to-Map Registration feature of ENVI was used to compare selected landmarks (e.g. bridges, airport runways) on a HICO image with those viewed on a referenced ArcMap 10 GIS image of the estuary of interest to identify ground control points (GCPs). After adding at least three GPCs to the HICO image, ENVI calculated new coordinates for those points and predicted their associated root-mean-square (RMS) errors. The RMS errors were errors inherent in finding the exact location of a feature in both HICO scene and reference scene. Points with high errors were removed and not used in the error analysis.

Each image was also warped and rotated in ENVI using 1st degree RST (rotation, scaling, and translation) with the nearest neighbour re-sampling method and saved as a shapefile. In Step 11, the georeferenced and warped R_{rs} images were imported into the ENVI Region of Interest (ROI) feature and overlain by GIS shapefiles created in ArcMap 10, which were representative of study estuaries. Using the ENVI ROI Tool the georeferenced R_{rs} values at each pixel in the image were extracted (clipped) and the clipped values saved as ACSII files for import into EXCEL.

2.5. *HICO Chlorophyll a model*

Using the dark pixel corrected R_{rs} data from images of Pensacola Bay (June, August, and September 2011), optimal spectral bands were identified in the red and NIR wavelengths to retrieve Chl *a* concentrations from HICO images using the three-band approach applied by Dall'Olmo et al. (2005) and Gitelson et al. (2008) to Case 2 waters.

In the approach, the model takes the form of $[R_{rs}(\lambda_1)^{-1} - R_{rs}(\lambda_2)^{-1}] * R_{rs}(\lambda_3)$ where the reciprocal of R_{rs} from two wavelengths (λ_1, λ_2) in the NIR to red spectrum is multiplied by reflectance of an NIR band (λ_3) (Gitelson et al. 2011; Moses et al. 2009; Dall'Olmo, Gitelson, and Rundquist 2003; Gons 1999; Gower, Doerffer, and Borstad 1999; Gitelson 1992). The approach assumes that (1) CDOM and detrital absorption at λ_2 are close to those at λ_1; (2) $R_{rs}(\lambda_3)$ is influenced by backscatter only, with minimal influence from water constituent absorption; and (3) backscatter ($b_b(\lambda)$) is approximately equal to the three wavelengths (Le et al. 2013; Le et al. 2010). From a bio-optical perspective, the three-band approach $[R_{rs}(\lambda_1)^{-1} - R_{rs}(\lambda_2)^{-1}]R_{rs}(\lambda_3) \approx [a_{ph}(\lambda_1) + a_w(\lambda_1) - a_w(\lambda_2)]/a_w(\lambda_3)$, where a_{ph} equals phytoplankton absorption and a_w equals absorption due to water (Le et al. 2013, 2009). Wavelength λ_1 is the most sensitive to absorption by Chl *a*. A second wavelength (λ_2), which is located close to λ_1, is minimally sensitive to Chl *a* absorption and corrects for absorption effects by other optically active constituents and the third wavelength (λ_3) is minimally sensitive to absorption by pigments, mineral particles, organic detritus, and CDOM (Gitelson et al. 2011; Hunter et al. 2010; Le et al. 2009).

Gitelson et al. (2008, 2011), Moses et al. (2009) Gitelson, Schalles, and Hladik (2007), and Dall'Olmo and Gitelson (2006) validated this approach using MERIS and

MODIS satellite data to estimate Chl *a* in productive coastal waters with concentrations between 20 and 40 μg l^{-1}. The approach has also be validated over a wide range of chlorophyll values (2–50 μg l^{-1} with an RSME <5.1 μg l^{-1} and 2–20 μg l^{-1} with an RSME <1.7 μg l^{-1}) using a MERIS three-band model by Gitelson et al. (2009).

The optimal spectral bands were determined through an iterative process using R_{rs} values from 657 to 749 nm (HICO bands 45–61) using HyperSAS data (660–735 nm) from five locations sampled during cruises FE1106 (June 2011) in Pensacola Bay and laboratory-measured Chl *a* values from those stations. Initially at each station, the position of λ_1 was determined using R_{rs} values at 703 and 735 nm set as placeholders for λ_2 and λ_3, respectively. These values along with R_{rs} values from $657 \geq \lambda_1 \leq 674$ nm were input into the three-band form to predict Chl *a* concentrations for Bands 45–48. The difference between measured and predicted Chl *a* concentrations at each wavelength was derived and the root-mean-square error (RSME) of Chl *a* estimation (Gitelson et al. 2008) determined using Equation (8).

The HyperSAS band with the lowest RMSE in the wavelength range was selected as the position for λ_1. To determine the position of λ_2, the location of the previously determined λ_1 and the set position of λ_3 (735 nm) were used to again predict Chl *a* concentrations from 703 to 730 nm. The difference between predicted and measured values was derived and RMSE determined. The HyperSAS band in this portion of the spectrum with the lowest RMSE in the wavelength range was selected as the optimal position for λ_2. Finally, λ_3 was determined using R_{rs} values from the previously determined wavelengths for λ_1 and λ_2. Chl *a* values predicted from R_{rs} values from 730 to 735 nm were compared with measured Chl *a* values to derive RSME values. The band with the lowest RSME in this range was selected as the position for λ_3.

RMSE values of the predicted Chl *a* concentrations were calculated from the following equation:

$$\mathrm{RMSE}\left(\mu g\ l^{-1}\right) = \frac{\sqrt{\left(\sum \mathrm{Chl}a_{\mathrm{measured}} - \mathrm{Chl}a_{\mathrm{predicted}}\right)^2}}{N-1,} \tag{8}$$

The HICO Chl *a* model was derived using R_{rs} values from Pensacola Bay images acquired on 2 June, 26 August, and 9 September 2011 using the optimized wavelengths derived from the HyperSAS datasets. These values were regressed against *in situ* chlorophyll *a* concentrations from stations in Pensacola Bay sampled concurrently with the ISS overpass to produce a regionally specific algorithm. Comparisons were made between the measured chlorophyll values and predicted chlorophyll concentrations to identify outliers and algorithm accuracy. Outliers in the dataset were identified using the quartile method (NIST/SEMATECH 2012) and removed. The accuracy of the algorithm was determined from the coefficient of determination, R^2, using Model II linear regression analysis (Laws 1997).

2.6. HICO turbidity model

An empirical relationship was derived between *in situ* turbidity (NTU) from stations in Pensacola Bay (June 2011) and R_{rs} at HICO band 43 ($R_{rs}(646)$). Turbidity was derived from HICO images using the approach of Chen, Hu, and Muller-Karger (2007), which was previously applied to MODIS/Aqua 250 m imagery from the Tampa Bay, FL, estuary. The accuracy of the turbidity algorithm was assessed by calculating the RMSE of the predicted turbidity and the measured turbidity from the stations in St Andrews Bay

during April and June 2010 and in Choctawhatchee Bay using the AED REMUS during August 2011.

2.7. HICO coloured dissolved organic matter absorption model

The absorption of light due to coloured dissolved organic matter was determined following the basic precepts of studies conducted by Bowers et al. (2000, 2004), Binding and Bowers (2003), and Tiwari and Shanmugam (2011). In this approach, CDOM absorptions at 412 nm ($a_{\mathrm{CDOM\ 412}}$) data from Pensacola Bay (June, August, and September 2011) were regressed against the ratio of waveband reflectance in the red (670 nm) and blue-green (490 nm) as measured from HICO R_{rs} from those waters to derive an empirical algorithm. Error was assessed by calculating the RMSE of the predicted and measured values from a subset of stations sampled in Pensacola Bay during June and September 2011 and stations sampled in Choctawhatchee Bay during July 2011.

3. Results and discussion

3.1. Image processing: geolocation

Using HICO scenes with obvious landmarks, GCPs were indentified on each image-based georeferenced ArcMap 10 scenes. Using coordinates from the ArcMap scenes, GCPs (and their RMS errors) were predicted for each HICO scene. Results indicated that an average of six ground control points was needed for accurate geolocation. RMS errors ranged from 0.7 to 3.2 m for Choctawhatchee Bay HICO images, from 0.7 to 2.8m for Pensacola Bay HICO images, from 0.5 to 1.1 m for St Andrews Bay images, and from 0.6 to 1.1 m for St Joseph's Bay HICO images. Although the number of GCPs was small, the predicted RMS errors are well below the 100 m pixel size of HICO images.

3.2. Image processing: Sun glint correction

As stated previously, all images were processed to remove the glint radiance caused by changing solar/viewing geometries of the HICO sensor. An example of the result of the Goodman, Lee, and Ustin (2008) approach is shown in Figure 4, which is from a pixel in an 8 January 2012 HICO image from Choctawhatchee Bay. In this figure, the uncorrected spectrum shows radiance values well into the NIR, which suggested that the entire spectrum was affected by Sun glint. After processing, the shape of the corrected radiance spectrum at that pixel has been preserved, compared to the original spectrum, and radiance values beyond 750 nm approach zero, which is in agreement with the assumption that NIR light is strongly absorbed by water and any signals reflected represent Sun glint reflected from the sea surface.

3.3. Image processing: atmospheric corrections and remote-sensing reflectance

A HICO image of Pensacola Bay acquired on 2 June 2011 was processed using the NRL/APS programme configured with the standard SeaDAS routines and then using wavelengths convolved to MODIS multispectral bands; ENVI FLASSH programme; and dark pixel subtraction approach for atmospheric correction evaluations. The resulting spectral signatures were compared with HyperSAS signatures from 21 stations occupied during the ISS overpass.

Figure 4. An example of the effect of the Sun glint correction routine on HICO Level 1b radiance data from Choctawhatchee Bay.

HICO hyperspectral images processed using the NRL/APS in SeaDAS mode and the ENVI FLASSH atmospheric correction programme did not yield satisfactory results and did not match any of the classic Case 2 spectra characteristic of the HyperSAS spectra from Pensacola Bay. HICO spectral signatures produced with the NRL/APS generally were under-corrected in the blue-green spectrum (Figure 5). The under-correction could be the result of noise in the NIR portion of the spectrum, polarization sensitivity, and/or sensor mis-calibration at blue wavelengths (400–450 nm). To help resolve these issues, vicarious calibration techniques are under development (Lewis et al. 2013). In contrast, all the MODIS multispectral values agreed very well with the HyperSAS spectra (n = 42; R^2 = 0.89; Figures 5 and 6), indicating that the problems lie with the HICO data and not with the NRL/APS atmospheric correction approach.

Spectral signatures corrected to remove atmospheric effects with the hyperspectral module of ENVI FLASSH also did not yield satisfactory results or match the shape of any HyperSAS spectral signatures (Figure 7). The entire spectrum was either over-corrected in the blue-green spectrum (e.g. PB18: Redfish Cove) or under-corrected in the red/NIR region (e.g. PB11: Blackwater Bay). FLAASH is very easy to use, if the user is able to specify appropriate input parameters that characterize the atmospheric conditions and illumination geometry at the time of image acquisition (Moses et al. 2012). The input parameters that describe the atmosphere serve as initial values for an iterative process in which atmospheric correction occurs. If actual information is not available, the user can input default values (ENVI 2009).

These problems encountered in this study may be related to errors in the locations of band centre wavelengths for the HICO sensor when these data are processed using ENVI FLASSH and problems with the illumination geometry at the time of image acquisition. The misidentification of band centre positions has been known to introduce significant

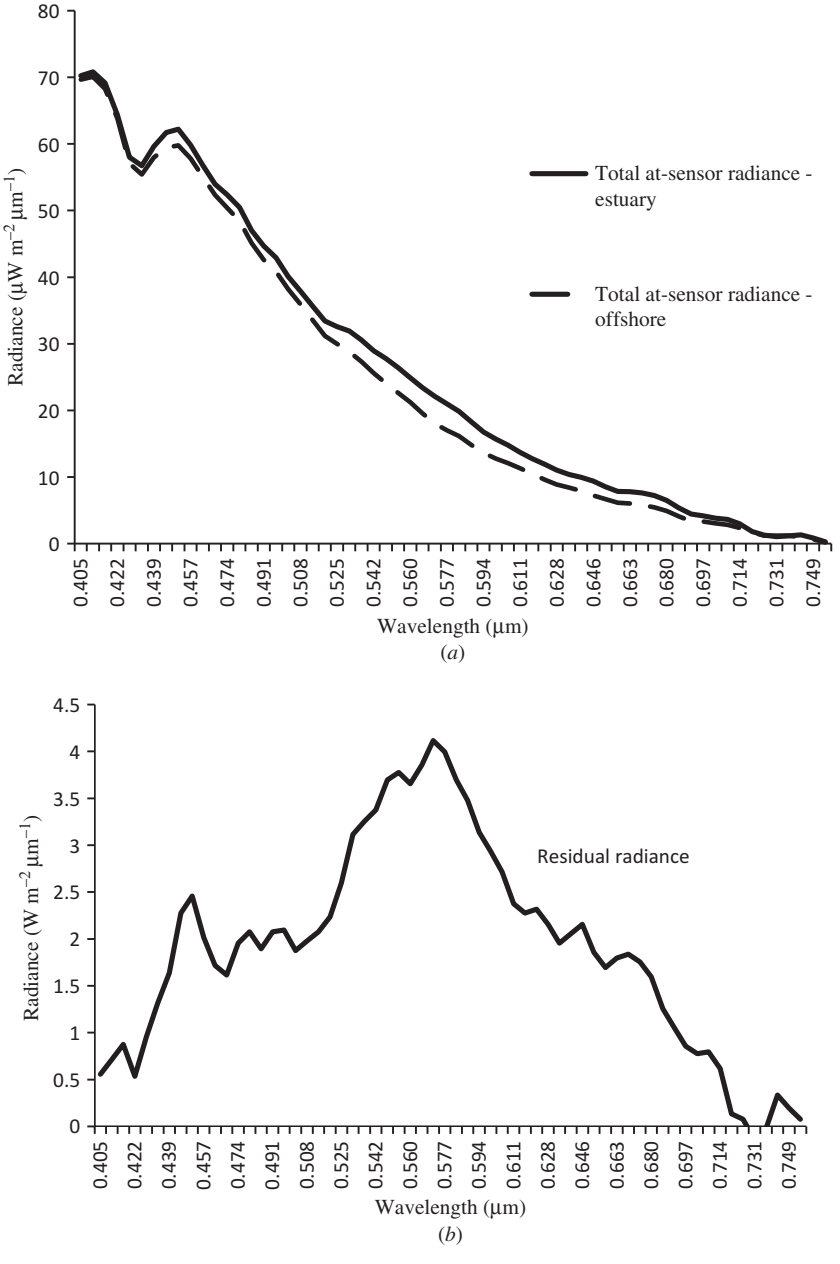

Figure 5. (*a*) Example of the at-sensor total radiance spectra for Pensacola Bay and near-shore Gulf of Mexico (GOM) waters; (*b*) The residual radiance spectra derived from subtracting the 'darker spectrum' of the GOM waters from the 'brighter' waters of Pensacola Bay using the dark pixel subtraction approach. The residual spectrum is the spectrum characteristic of Case 2 waters.

errors into the retrieval of the water signal (ENVI 2009). ENVI FLASSH attempted to minimize these errors through a utility that automatically identified and corrected wavelength mis-calibrations using sensor-specific spectrograph definition files. These files are assigned specific spectral features that are used to correct the wavelength calibrations. For

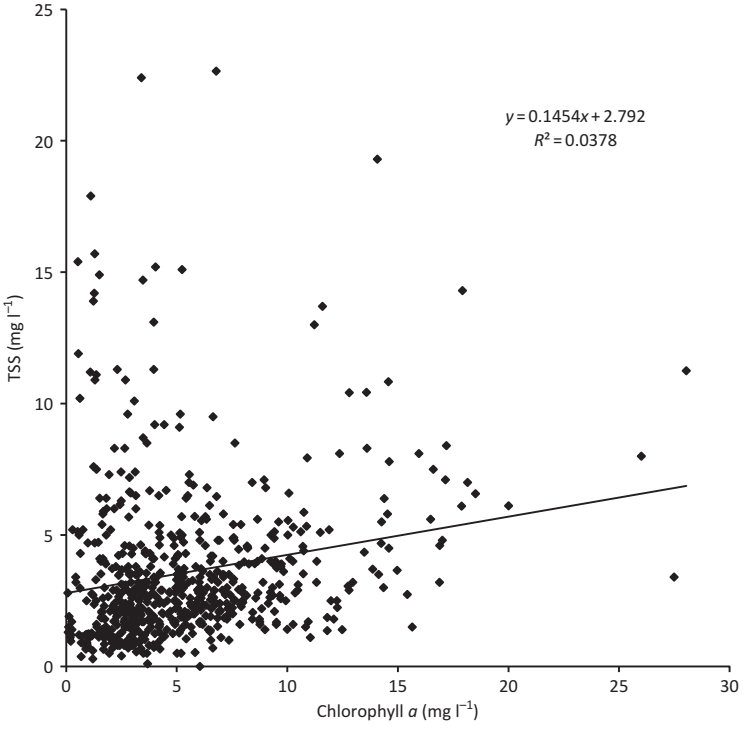

Figure 6. TSS concentrations *versus* Chl *a* concentrations (n = 641) in Pensacola Bay, St Andrews Bay, Choctawhatchee Bay, and St Joseph Bay from October 2009 to September 2011. The low determination coefficient for linear relationship (R^2) indicated TSS and chlorophyll are practically independent, which is characteristic of Case 2 waters.

example, when AVIRIS data are processed, FLASSH used the oxygen feature at 760.17 nm as the reference absorption feature and the CO_2 feature at 2058.7 nm as well as the full-width at half-maximum (FWHM) associated with these features to identify the bands needed for atmospheric correction. Spectral definition files for AVIRIS, HYDICE, HYMAP, HYPERION, CASI, and AISA sensors are included as part of the processing package and when accessed automatically recalibrate wavelength errors for these sensors. However, files specific to the HICO sensor are not included in this sensor suite, forcing the use of generic hyperspectral wavelength calibrations included in the software package or the creation of a sensor spectrograph definition file based on sensor characteristics.

Moreover, in the header file of each HICO image, the user is cautioned that the image view and solar view geometries are approximate and do not account for ISS attitude. These approximations created problems with accurately defining the zenith and azimuth angles. Because of these complications, ENVI FLAASH was not used to atmospherically correct HICO images.

In contrast, HICO images processed using the dark pixel subtraction approach yielded matchups that spectrally corresponded very well with the HyperSAS signatures (Figure 8). Exceptions to this general observation are seen in the spectra from PB07: Pensacola Bay and PB24: Pensacola Bay, which are under-corrected in the blue portion of the spectrum. This approach does not require sensor-specific information for processing and corrects for

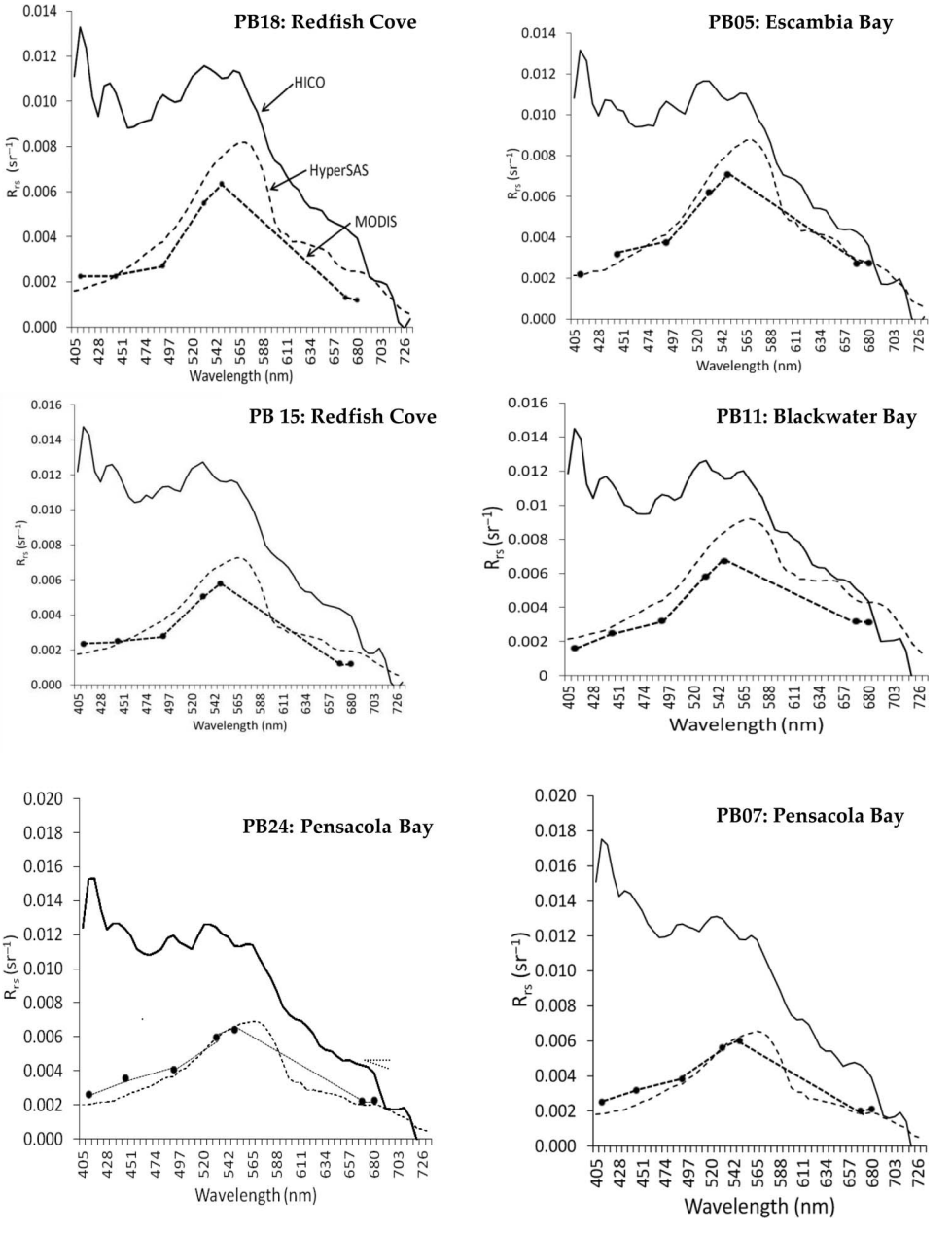

Figure 7. Examples of HICO (solid line) and MODIS (dotted line) spectral signatures processed using the NRL automated processing system (APS) from six stations in the Pensacola Bay system retrieved from the 2 June 2011 HICO image and compared with HyperSAS (dashed line) values. Please note these signatures were not corrected for seabed reflectance

mis-calibration and/or noisy data on a scene-by-scene basis. The correction occurs because any inherent problems in the deep-water and near-shore spectral sets are removed through subtraction, leaving only the difference spectra. Thus, this inherent difference might account for the improved spectral matchups using the dark pixel atmospheric

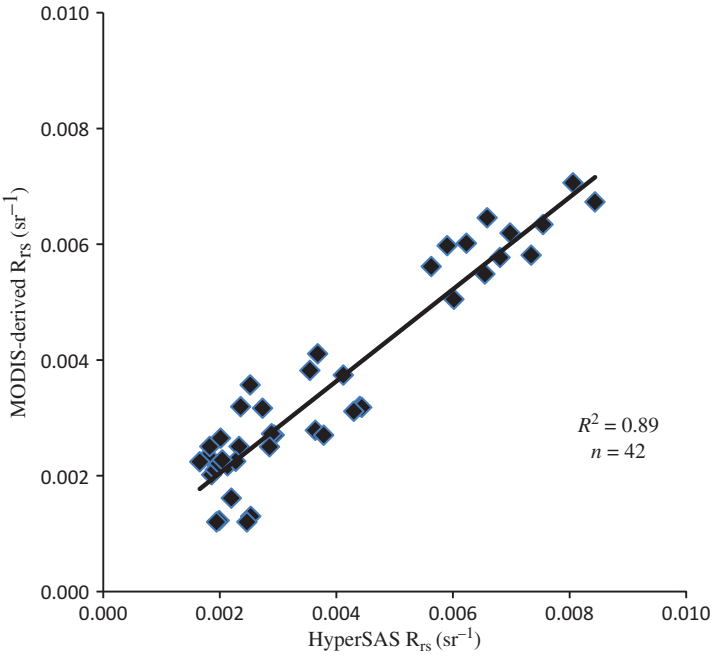

Figure 8. MODIS R_{rs} derived from NRL/APS compared to HyperSAS R_{rs}.

correction method, compared to the matchups produced using the APS and FLAASH approaches.

Sensor-specific information is not required for this type of atmospheric correction because removing the contribution of atmospheric backscattering from the at-sensor radiance curve is not dependent on the precise location of spectral channels for water vapour and absorption features. Spectrally, the at-sensor radiance curves of image pixels reflected the shape of the solar irradiance curve with atmospheric Rayleigh scattering and fell off roughly as λ^{-4}. 'Dark pixels' are assumed to not scatter photons as much as land or 'brighter' waters with sediments. It was also assumed that by subtracting the at-sensor 'dark pixel' radiance from the at-sensor spectra of 'bright' pixels, the spectra produced had Rayleigh scattering effects removed and contained primarily photons scattered from the constituents within the water column (Figure 9). This approach was selected as the method for atmospherically correcting the remaining HICO images. However, with the dark pixel subtraction approach, there was a concern as demonstrated in previous studies – the subtraction process could create an over-correction, which results in negative R_{rs} values in the blue portion of the spectrum (Moses et al. 2009; Palandro 2006). To address this issue, an offset (avg 0.003 sr^{-1}) determined by R_{rs} values at 450 nm was applied to the spectra to adjust reflectance values so as to yield positive values in the blue portion of the spectrum (Hu et al. 2004).

3.4. *Algorithm development and tuning for estimating chlorophyll* a

In general, the waters sampled had Chl *a* concentrations, total suspended sediment (TSS) concentrations, and turbidity values that varied by more than a factor of 10 (Table 2). TSS

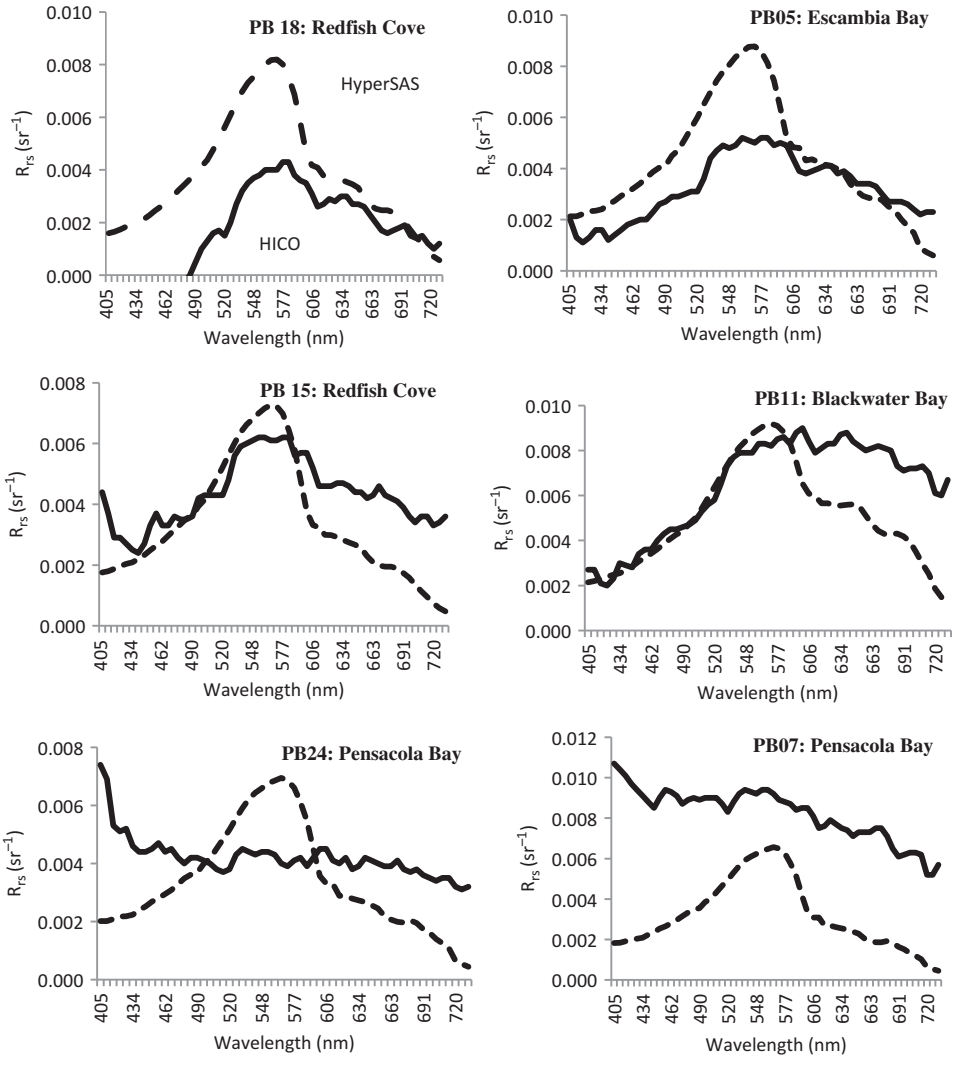

Figure 9. Examples of spectral signatures processed using ENVI FLASSH from six stations in the Pensacola Bay system retrieved from the 2 June 2011 HICO (solid line) image and those collected using HyperSAS (dashed line). Note that these signatures were not corrected for seabed reflectance.

Table 2. Descriptive statistics for optical water-quality parameters for Pensacola, Choctawhatchee, St Andrews, and St Joseph Bays from October 2009 to September 2011.

		N	Min	Max	Median	Mean	STD
Chl *a*	$\mu g\ l^{-1}$	640	0.07	28.04	4.40	5.41	3.94
TSS	$mg\ l^{-1}$	640	0.00	22.65	2.80	3.58	2.95
Turbidity	NTU	46	0.13	4.75	0.85	1.08	0.83
$a_{CDOM(412)}$	m^{-1}	715	0.13	17.20	1.41	2.28	2.42

Notes: *N*, number of samples; $a_{CDOM(412)}$, CDOM absorption at 412 nm; STD, standard deviation of measurements.

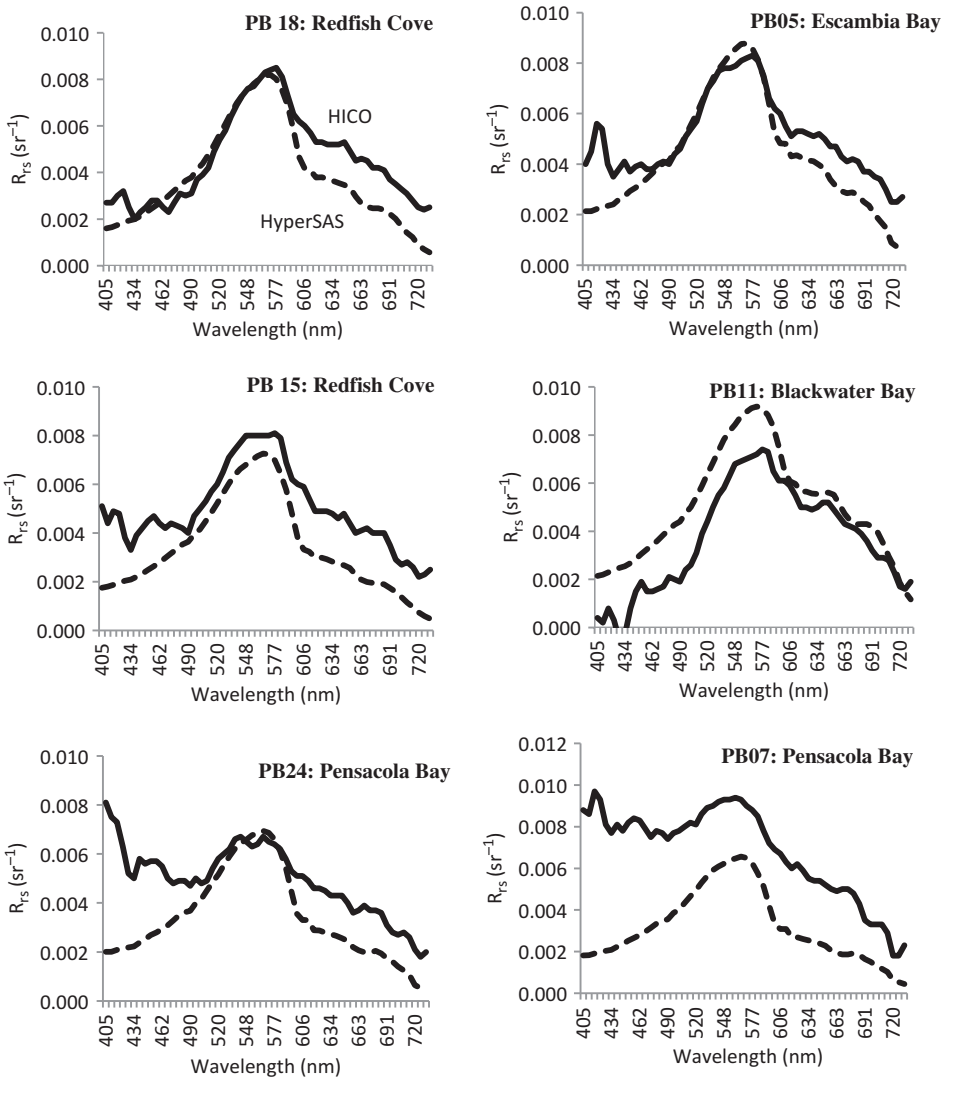

Figure 10. Examples of spectral signatures processed using the dark pixel subtraction approach from six stations in the Pensacola Bay system retrieved from the 2 June 2011 HICO (solid line) image and those collected using HyperSAS (dashed line). Note that these signatures were not corrected for seabed reflectance.

concentrations correlated weakly with Chl *a* measurements (Figure 10), confirming that the waterbodies sampled during this study belong to Case 2 waters (Morel and Prieur 1977). This suggested that algorithms commonly used for estimating Chl *a* concentrations in Case 1 ocean waters (e.g. O'Reilly et al. 1998) are inadequate for accurate estimations in these Case 2 waters.

Using an optimization procedure, a three-band empirical model was developed using HyperSAS spectral data and laboratory-extracted Chl *a* concentrations from Pensacola Bay (June, August, and September 2011) to estimate Chl *a* concentrations from the HICO images.

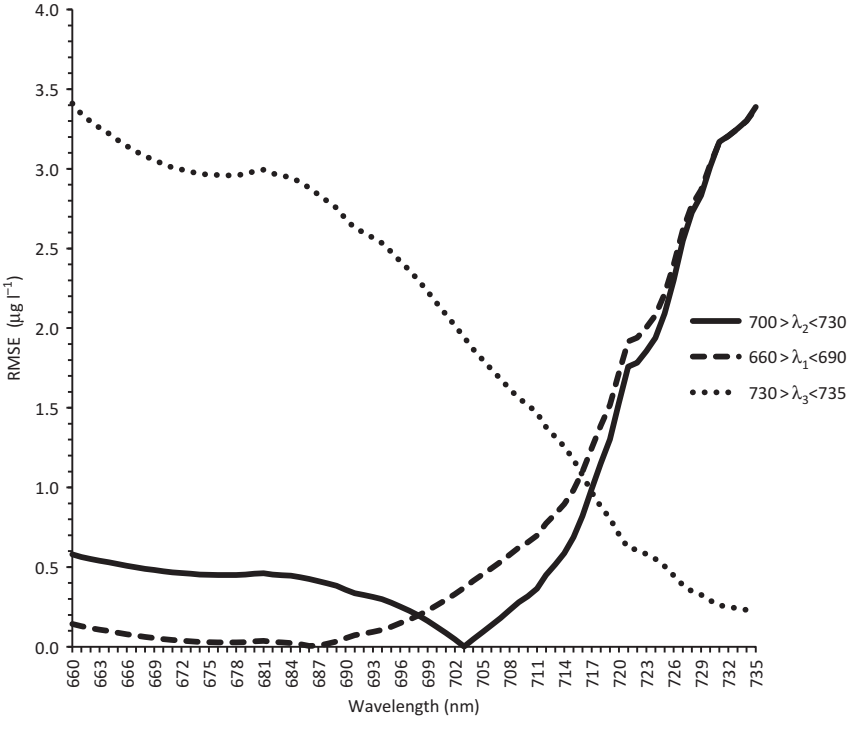

Figure 11. Line plots of the root-mean-square error of Chl *a* from HyperSAS hyperspectral data and measured Chl *a* at different wavelengths. Minima occurred at 686 nm for λ_1 (RMSE = 0.002 µg l^{-1}), at 703 nm for λ_2 (RMSE = 0.006 µg l^{-1}), and at 735 nm for λ_3 (RMSE = 0.217 µg l^{-1}), which correspond to HICO bands 50, 73, and 58.

The optimal position of λ_2 was derived by setting λ_1 and λ_3 at 660 and 735 nm, respectively, with the minimal RMSE (0.002 µg l^{-1}) occurring at 703 nm (Figure 11, solid line). To determine the optimal position of λ_1, λ_2 was set at 703 nm and λ_3 was set at 735 nm. Using this combination, the minimum RMSE (0.006) was located at 686 nm (Figure 11, dashed line). To determine λ_3, the 686 and 703 nm bands were selected for λ_1 and λ_2, respectively, with the minimal RMSE (0.217) occurring at 735 nm (Figure 11, dotted line).

With the optimal bands identified, spectral values at 686 (HICO band 50), 703 (HICO band 53), and 735 nm (HICO band 58) from HICO images were used to derive the ratio values that were proportional to Chl *a* concentration (Gitelson et al. 2011; Hunter et al. 2010; Le et al. 2009; Dall'Olmo and Gitelson 2006). These values were regressed against *in situ* Chl *a* concentrations from a total of 17 stations in Pensacola Bay sampled during June, August, and September 2011 to produce a regionally specific algorithm (Figure 12(*a*), Tables 3 and 4). The algorithm was validated using measured *in situ* Chl *a* samples collected from April 2010 to September 2011 at 21 stations in St Andrews Bay, Pensacola Bay, and Choctawhatchee Bay (Figure 12(*b*), Table 5).

The algorithm was applied to HICO images from the four estuaries, beginning in April 2010 and ending in May 2012, to map spatial and temporal changes in Chl *a* distribution during the period. Figure 15(*a*) represents the chlorophyll distribution within Choctawhatchee Bay from a HICO image acquired during fall 2011. This image shows

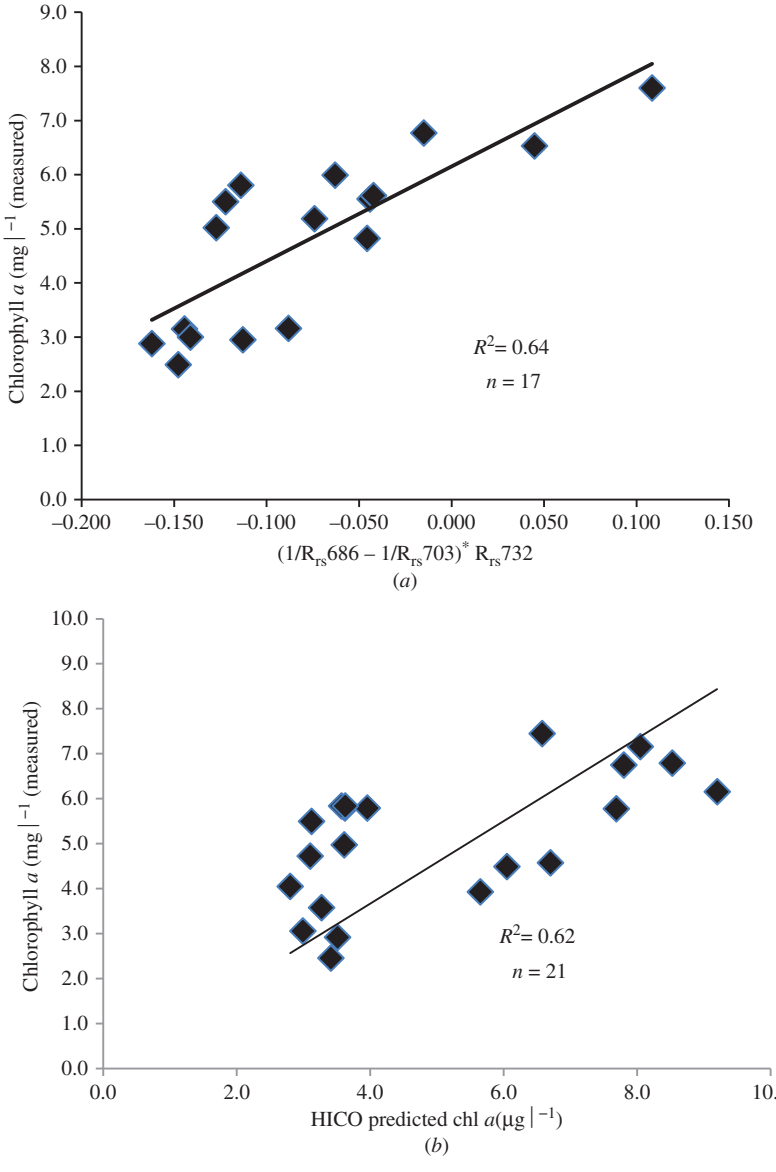

Figure 12. (*a*) Scatterplot of measured Chl *a* *versus* the three-band model values using R_{rs} values from HICO images acquired on 2 June, 26 August, and 9 September 2011 and estimates of extracted or fluorometer-derived Chl *a* from 17 stations sampled in Pensacola Bay; (*b*) Scatterplot of measured Chl *a* values *versus* HICO Chl *a* from St Andrews Bay (14 April 2010), Pensacola Bay (2 June 2011 and 9 September 2011), and Choctawhatchee Bay (24 August 2011).

a latitudinal gradation in Chl *a* with higher values in the western bay near the tidal inlet connection to the Gulf of Mexico and lower Chl *a* in the east near the entrance to the Choctawhatchee River (Figure 1). At smaller spatial scales, the high pixel resolution of HICO also captured the Chl *a* distribution in the surrounding, smaller embayments.

Table 3. Descriptive statistics of samples (n = 17) used in deriving the three-band HICO chlorophyll model.

Date	Station	Chl *a* (measured)	Min (μg l^{-1})	Max (μg l^{-1})	Median (μg l^{-1})	Mean (μg l^{-1})	STD (μg l^{-1})
2 June 2011	PB04	5.5	2.5	7.6	5.2	4.8	1.6
2 June 2011	PB05	3.0					
2 June 2011	PB07	2.9					
2 June 2011	PB08	6.5					
2 June 2011	PB12	5.0					
2 June 2011	PB13	3.2					
2 June 2011	PB14	3.2					
2 June 2011	PB17	3.0					
2 June 2011	PB18	2.5					
26 August 2011	PB04	6.8					
26 August 2011	PB05	6.0					
26 August 2011	PB06	5.2					
26 August 2011	PB07	5.6					
26 August 2011	PB08	4.8					
26 August 2011	PB06	5.6					
9 September 2011	PB07	7.6					
9 September 2011	PB09	5.8					

Note: PB, Pensacola Bay; STD, standard deviation of chlorophyll concentrations.

Table 4. Algorithms derived to map the distribution of water-quality indicators derived from atmospherically corrected remotely sensed reflectances (R_{rs}). Also shown are the units of measurement; the slope (m) and goodness-of-fit (R^2) of the relationship between measured and predicted values; the number of values used (n) to derive the algorithm; and the root-mean-square error (RMSE) of the measurements.

Indicator	Model	m	R^2	n	RMSE
Chl *a* (μg l^{-1})	$17.477 \times [a] + 6.152\ a = [1/R_{rs}(686) - 1/R_{rs}(703)] \times R_{rs}(735)$	1.40	0.62	21	1.7
Turbidity (NTU)	$2 \times 10^6 \times [R_{rs}(646)^{2.7848}]$	1.21	0.67	19	0.6
$a_{CDOM412)}$ (m^{-1})	$0.8426 \times [R_{rs}(670)/R_{rs}(490)] - 0.032$	0.90	0.93	18	0.2

It is well known that estuaries are highly dynamic interfaces where phytoplankton dynamics can change over tidal cycles. To observe Chl *a* variability associated with sampling at different times relative to an ISS overpass, we examined the goodness-of-fit between measured and predicted Chl *a* values as a function of time after an ISS overpass. Chl *a* samples collected within four hours of an overpass were assessed from stations in Pensacola Bay, Choctawhatchee Bay, and St Andrews Bay sampled during April 2010 and June to August 2011. A strong relationship (R^2 = 0.62, p < 0.001, RMSE = 1.7 μg l^{-1}) existed for stations (n = 21) occupied 0–4 hours of an overpass (Figure 12(*b*), Table 5).

Chl *a* values were also derived using the OC3 SeaDAS algorithm with HICO data (processed through NRL/APS). These estimates were compared with NRL glider chlorophyll values collected on 28 October 2011 along the inner continental shelf waters off

Table 5. Descriptive statistics of samples (n = 21) used to validate the three-band HICO chlorophyll model.

Date	Station	Chl *a* (measured)	Min (μg l^{-1})	Max (μg l^{-1})	Median (μg l^{-1})	Mean (μg l^{-1})	STD (μg l^{-1})
14 April 2010	SA02	7.7	2.8	9.2	3.6	5.1	2.2
14 April 2010	SA08	9.2					
2 June 2011	PB06	3.0					
2 June 2011	PB11	5.7					
2 June 2011	PB19	3.1					
2 June 2011	PB20	3.3					
2 June 2011	PB21	2.8					
2 June 2011	PB22	3.4					
2 June 2011	PB23	6.7					
2 June 2011	PB24	3.5					
30 July 2011	CH01	3.1					
30 July 2011	CH02	3.6					
30 July 2011	CH03	3.6					
30 July 2011	CH05	4.0					
30 July 2011	CH06	3.6					
30 July 2011	CH07	3.6					
24 August 2011	CH07	6.0					
9 September 2011	PB02	7.8					
9 September 2011	PB03	8.0					
9 September 2011	PB04	8.5					
9 September 2011	PB05	6.6					

Note: SA, St Andrews Bay; PB, Pensacola Bay; CH, Choctawhatchee Bay; STD, standard deviation of chlorophyll concentrations.

Pensacola Bay. The OC3 values were generally higher than the glider values and approximately constant at 1.3 μg l^{-1} with very low variability (data not shown).

A unique opportunity occurred on 28 October 2011 when a clear MODIS scene was acquired within 7 min before the HICO overpass. Using the NRL/APS, the OC3 algorithm Chl *a* and standard SeaDAS atmospheric correction were applied to both HICO image and MODIS scene (Figure 13(*a*)). During processing, the 1 km MODIS image was re-sampled to the 100 m HICO pixel size and the HICO image was georeferenced to the 'new' MODIS image. A region-of-interest (ROI) was generated near the mouth of Pensacola Bay and all MODIS and HICO chlorophyll values within that ROI were extracted from the two scenes. During the re-sampling process on the MODIS scene, pixels were simply replicated to increase the resolution from 1 km to 100 m. For example, if a 1 km MODIS pixel had a value of 1 μg l^{-1} then there are now 100 pixels with that same value for the comparison to HICO. Results showed there was agreement between the HICO and MODIS OC3 Chl *a* values than between the HICO and glider values (m = 0.38; intercept = 0.81; R^2 = 0.85; Figure 13(*b*)). The high R^2 value indicated there is a strong linear relationship between the two variables (i.e. the proportion of the variance in the HICO Chl *a* values is accounted for by the MODIS Chl *a* values). However, the non-zero intercept and the bias (slope not equal to 1) indicated that the MODIS and HICO values are not necessarily close to each other. For example, HICO values were somewhat higher than MODIS values at Chl *a* concentrations below 1.2 μg l^{-1}, and lower than MODIS at concentrations above 1.2 μg l^{-1}. The significant regression of OC3 results from HICO and MODIS retrieved by the NRL/APS indicated that other algorithms in the SeaDAS processing package could be applied to leverage the high spatial resolution

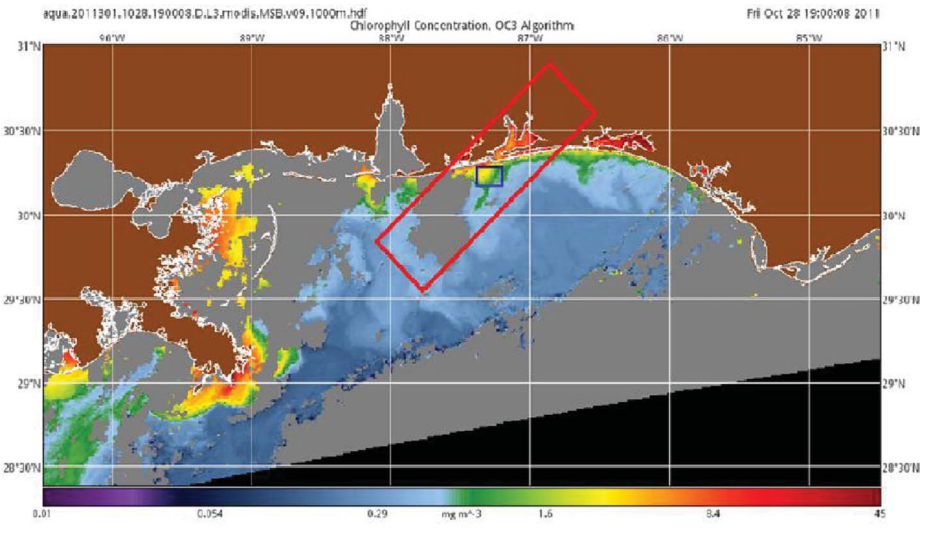

(*a*)

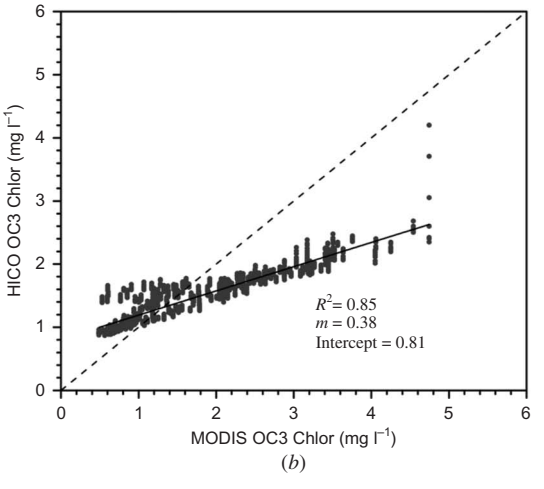

(*b*)

Figure 13. (*a*) HICO and MODIS Chl *a* concentrations (processed through NRL/APS using the OC3 Chl *a* algorithm) on 28 October 2011, offshore of Pensacola Bay. The red rectangle overlaid on the MODIS image from 1900 GMT represents the location of a coincident HICO scene from the same day at 1907 GMT. The blue rectangle indicates the pixels included in the matchup comparison. (*b*) HICO Chl *a* concentrations *versus* MODIS Chl *a* values on 28 October 2011, offshore of Pensacola Bay; the dashed line corresponds to the 1:1 line.

capability of HICO relative to 1 km MODIS data if the appropriate atmospheric corrections could be implemented.

3.5. Turbidity and CDOM models

Turbidity is a fundamental indicator of water clarity that is a measure of the ability of suspended material to diminish the penetration of light in aquatic systems (AGI 1974).

Variations in turbidity help trace the distribution of total suspended sediments, which are affected by geological processes (e.g. coastal erosion) and the mobilization of pollutants (Zhang et al. 2011; Heyes, Miller, and Mason 2004). Turbidity can vary widely spatially and temporally in coastal and estuarine waters. This variability results in the failure of conventional sampling methods to accurately characterize turbidity dynamics because of limitations in temporal and spatial sampling schemes. We empirically derived a water clarity algorithm (Table 4) by regressing *in situ* turbidity measured from 18 stations in Pensacola Bay on 2 June 2011 against R_{rs} retrieved at 646 nm from a HICO image acquired on that day (Table 6). In the approach, R_{rs} is assumed to be proportional to backscatter (b_b), which is equivalent to turbidity for medium to low turbid waters (Chen, Hu, and Muller-Karger 2007). Figure 13(*a*) shows that HICO $R_{rs}(646)$, which ranged from 0.003 to 0.009 sr^{-1}, was closely related ($R^2 = 0.72$) with *in situ* turbidity values from 0.10 to 10 NTU (Figure 14(*a*)). The model was validated using *in situ* turbidity measurements from 14 stations in St Andrews Bay (from April and June 2010) and the REMUS AUV from two locations along a track in Choctawhatchee Bay on August 2011 (Table 7). Chen, Hu, and Muller-Karger (2007) suggested that the approach should be applicable to other estuaries where CDOM contribution is negligible at the 646 nm wavelength. This observation was confirmed as results showed a strong relationship ($R^2 = 0.67$; $p < 0.001$; RMSE = 0.56 NTU) between measured and predicted values (Figure 14(*b*)). This relationship was consistent with turbidity values from Tampa Bay, FL. An example image from St Andrews Bay acquired during spring 2011 is provided in Figure 15(*b*). St Andrews Bay generally has turbidity values from 0.2 to 2.3 NTU. Higher turbidity (2.4–12.9 NTU) was observed in isolated areas usually associated where streams enter embayments and along the tidal inlet.

Table 6. Descriptive statistics of samples ($n = 18$) used in deriving the HICO Turbidity model.

Date	Station	Turbidity (measured)	Min (NTU)	Max (NTU)	Median (NTU)	Mean (NTU)	STD (NTU)
2 June 2011	PB03	4.75	0.55	4.75	1.02	1.36	0.99
2 June 2011	PB04	1.78					
2 June 2011	PB05	0.99					
2 June 2011	PB06	1.71					
2 June 2011	PB07	0.55					
2 June 2011	PB08	0.85					
2 June 2011	PB11	1.56					
2 June 2011	PB12	0.94					
2 June 2011	PB13	1.03					
2 June 2011	PB14	0.75					
2 June 2011	PB15	1.60					
2 June 2011	PB16	1.02					
2 June 2011	PB17	0.65					
2 June 2011	PB18	1.11					
2 June 2011	PB19	0.85					
2 June 2011	PB20	0.86					
2 June 2011	PB21	1.24					
2 June 2011	PB22	2.90					
2 June 2011	PB23	0.69					

Note: PB, Pensacola Bay; STD, standard deviation of turbidity measurements.

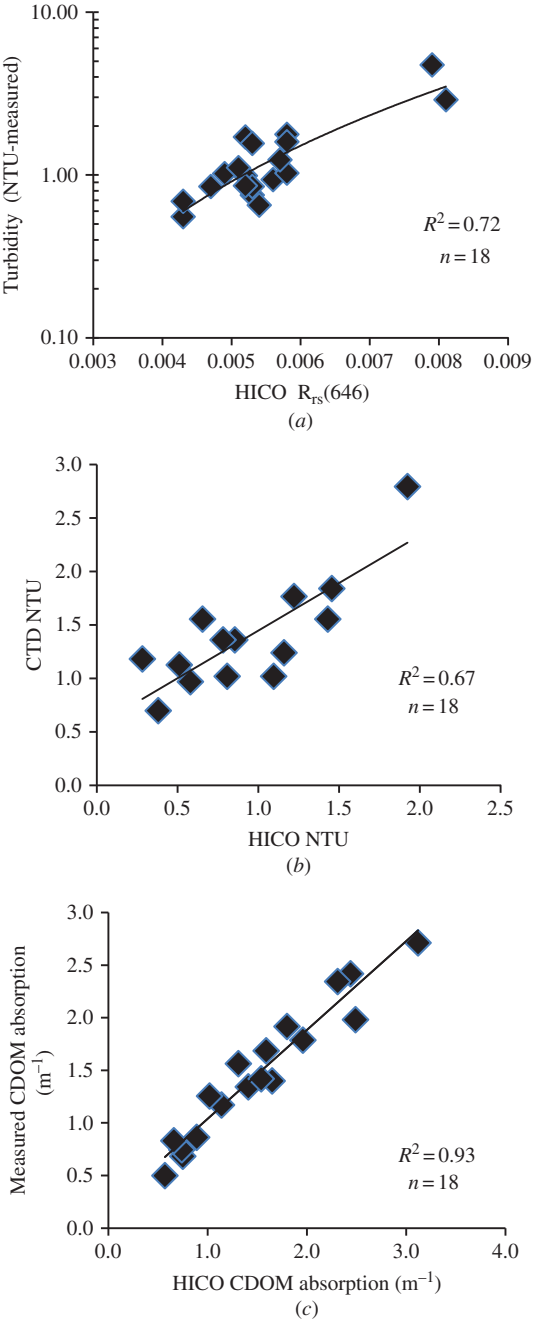

Figure 14. (*a*) Scatterplot of turbidity measured from CTD casts at stations in Pensacola Bay during 2 June 2011 and remotely sensed reflectance at 646 nm from the HICO image acquired on that day, (*b*) scatterplot of measured and predicted turbidities using *in situ* measurements from 12 stations in St Andrews Bay from April and June 2010 and the REMUS AUV from two locations (30.440N – 86.300 W and 30.439N – 86.304W) along a trackline in Choctawhatchee Bay on August 2011, and (*c*) scatterplot of CDOM light absorption at 412 nm measured during CTD casts from stations in the Pensacola Bay system during 11 June, 11 August, and 11 September 2011 *versus* CDOM light absorption at 412 nm predicted from HICO images acquired on those days.

Table 7. Descriptive statistics of samples (n = 14) used to validate the HICO turbidity model.

Date	Station	Turbidity (measured)	Min (NTU)	Max (NTU)	Median (NTU)	Mean (NTU)	STD (NTU)
14 April 2010	SA04	0.85	0.28	1.92	0.83	0.94	0.47
14 April 2010	SA05	0.38					
14 April 2010	SA07	0.65					
14 April 2010	SA08	0.58					
14 April 2010	SA10	1.09					
14 April 2010	SA11	1.92					
17 June 2010	SA02	1.22					
17 June 2010	SA04	0.81					
17 June 2010	SA05	0.51					
17 June 2010	SA08	0.28					
17 June 2010	SA10	0.78					
17 June 2010	SA11	0.75					
24 August 2011	CH-AUV	1.45					
24 August 2011	CH-AUV	1.43					

Note: SA, St Andrews Bay; CH-AUV, Choctawhatchee Bay REMUS data; STD, standard deviation of turbidity measurements.

Several studies have shown that CDOM primarily absorbs light in the UV and visible spectral range and plays a key role in controlling light attenuation and spectral quality in Atlantic and Gulf of Mexico estuaries (Keith, Yoder, and Freeman 2002; Chen et al. 2007; Tehrani et al. 2013). CDOM, the coloured fraction of dissolved organic matter (DOC), can be estimated by ocean sensors and can be utilized to estimate the standing stock of DOC and the carbon cycle in aquatic environments (Coble 2007). Monitoring the distribution of CDOM at several spatial and temporal scales could provide diagnostic information on the natural and anthropogenic factors affecting the capacity of these waters to provide sufficient sunlight to planktonic and macrophytic vegetation for photosynthesis and growth. Previously, D'Sa, Miller, and Del Castillo (2006) used *in situ* $a_{\mathrm{CDOM}(412)}$ measurements, collected with 14 hours of an overflight, and the ratio of $R_{\mathrm{rs}}(510)$ and $R_{\mathrm{rs}}(555)$ from SeaWiFS to derive an algorithm that mapped the surface values of CDOM absorption in the offshore waters of the northern Gulf of Mexico. Statistical analysis revealed the algorithm performed well with an R^2 of 0.66 and an RSME of 0.23 m^{-1}.

We empirically derived an algorithm to study CDOM distribution within estuarine waters of the Gulf coast (Table 4). The algorithm was derived by regressing *in situ* CDOM absorption measurements ($a_{\mathrm{CDOM}(412)}$), collected within five hours of an ISS overflight, at 17 stations in Pensacola Bay from June to September 2011 against the ratio of R_{rs} retrieved from 670 and 490 nm from HICO images acquired on those days (Table 8). This approach assumes that in order to retrieve CDOM remotely there is a robust relationship between the red/blue-green spectral ratio and the absorption of CDOM. The algorithm was validated using measured CDOM absorption values, also collected within six hours of an ISS overflight, from 18 stations in Pensacola and Choctawhatchee Bays (2 June, 30 July, and 9 September 2011; Table 9) and HICO images from those days. During this time period, $a_{\mathrm{CDOM412)}}$ varied spatially and temporally from 0.6 to 3.1 m^{-1}. A comparison of the measured *versus* predicted absorption values showed an excellent relationship (R^2 = 0.93, $p < 0.001$; Figure 14(*c*)) and an RMSE of 0.21 m^{-1}. Figure 15 (*c*) provides an example of the CDOM distribution in Pensacola Bay acquired during 16

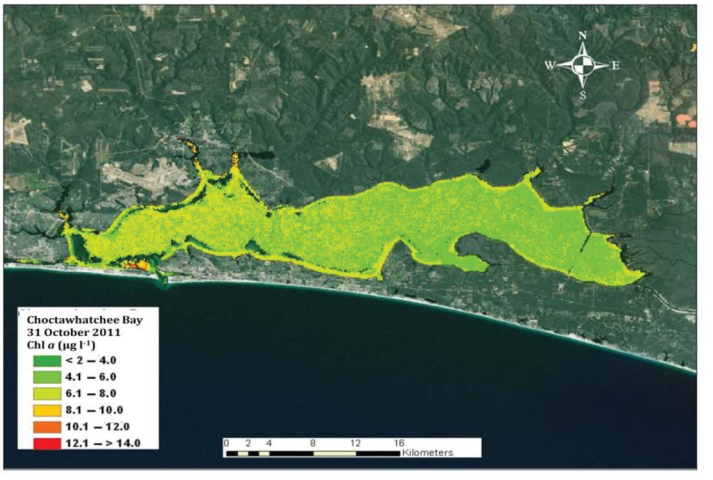

(*a*)

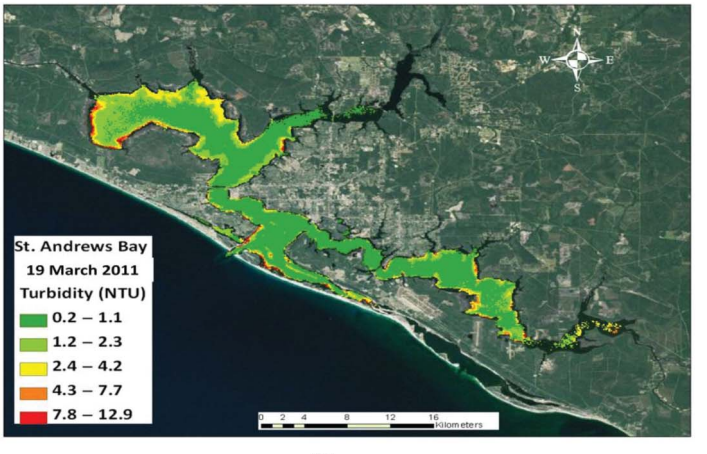

(*b*)

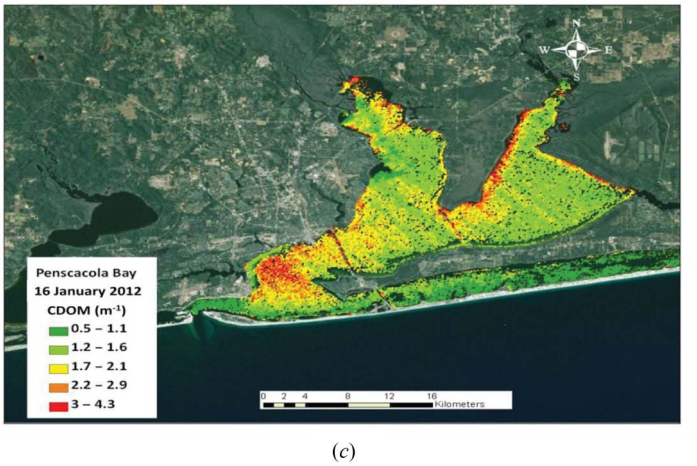

(*c*)

Figure 15. Example images of water-quality indicators derived from HICO atmospherically corrected data using the dark pixel subtraction approach: (*a*) Chl *a* distribution (Choctawhatchee Bay, 31 October 2011), (*b*) turbidity distribution (St Andrews Bay, 19 March 2011), and (*c*) CDOM distribution (Pensacola Bay, 16 January 2012).

Table 8. Descriptive statistics of samples (n = 17) used in deriving the HICO CDOM absorption model.

Date	Station	$a_{CDOM(412)}$ (measured)	Min (m^{-1})	Max (m^{-1})	Median (m^{-1})	Mean (m^{-1})	STD (m^{-1})
2 June 2011	PB04	1.08	0.63	2.03	1.08	1.19	0.43
2 June 2011	PB05	0.77					
2 June 2011	PB07	0.63					
2 June 2011	PB12	1.04					
2 June 2011	PB13	0.81					
2 June 2011	PB14	0.83					
26 August 2011	PB03	1.80					
26 August 2011	PB04	1.60					
26 August 2011	PB05	1.62					
26 August 2011	PB06	1.17					
26 August 2011	PB07	1.18					
26 August 2011	PB08	1.02					
26 August 2011	PB09	0.78					
9 September 2011	PB06	1.71					
9 September 2011	PB07	2.03					
9 September 2011	PB08	1.41					
9 September 2011	PB09	0.72					

Note: $a_{CDOM(412)}$, CDOM absorption at 412 nm; PB, Pensacola Bay; STD, Standard deviation of CDOM absorption measurements.

Table 9. Descriptive statistics of samples (n = 18) used to validate the HICO CDOM absorption model.

Date	Station	$a_{CDOM(412)}$ (measured)	Min (m^{-1})	Max (m^{-1})	Median (m^{-1})	Mean (m^{-1})	STD (m^{-1})
2 June 2011	PB03	1.08	0.57	3.12	1.48	1.52	0.73
2 June 2011	PB06	0.75					
2 June 2011	PB08	0.57					
2 June 2011	PB09	0.74					
2 June 2011	PB15	0.66					
30 July 2011	CH01	0.89					
30 July 2011	CH02	1.14					
30 July 2011	CH03	1.65					
30 July 2011	CH04	1.02					
30 July 2011	CH05	1.41					
30 July 2011	CH06	1.54					
30 July 2011	CH07	1.59					
30 July 2011	CH08	2.49					
30 July 2011	CH09	1.96					
9 September 2011	PB02	3.12					
9 September 2011	PB03	2.44					
9 September 2011	PB04	2.31					
9 September 2011	PB05	1.80					

Note: $a_{CDOM(412)}$, CDOM absorption at 412 nm; PB, Pensacola Bay; CH, Choctawhatchee Bay; STD, standard deviation of CDOM absorption measurements.

January 2012 (Figure 15(*c*)). This image showed the highest CDOM absorption (1.7–4.3 m^{-1}) in the vicinities of PB2 and PB3 in the upper parts of the Pensacola Bay system and PB12 and PB16 in eastern Pensacola Bay (Figures 2 and 15(*c*)). The most intense absorption was located in the vicinity of PB07, PB08, PB24, PB25, and PB26 in lower Pensacola Bay (Figures 2 and 15(*c*)).

4. Conclusions

HICO hyperspectral data were acquired from the surface waters of four Florida estuaries during overflights of ISS. Several water-quality algorithms were derived to estimate the indicators of ecological condition. The ~6 nm spectral resolution and ~95 m spatial resolution of HICO acquired images made this sensor unique among the previous and current ocean colour satellites. These attributes not only make HICO a unique tool for algorithm development in coastal waters, but also could provide future value for the monitoring and management of the nation's coasts in optically complex waters and areas below the spatial resolution of previous sensors. In our study, we found that the dark pixel atmospheric correction method worked very well in removing atmospheric effects from HICO images. Using atmospherically corrected HICO R_{rs} values and *in situ* and laboratory data from an extensive field sampling programme in the study estuaries, algorithms were created, and tested, which successfully estimated chlorophyll concentrations, light absorption due to CDOM, and water clarity as expressed by turbidity.

Although the potential benefits are many, there are several issues that must be resolved before HICO images and data can be incorporated into routine monitoring programmes to benefit decisions made by coastal managers. We suggest that HICO vicarious calibration and standardized atmospheric correction issues must be resolved, and work is under way on these (Lewis et al. 2013). During our analysis, we observed that multiple images of the same target did not cover identical spatial coordinates and resulted in spatial offsets >10 km. This issue may result from the differences between the actual and predicted ISS ephemeris data, which impacts the times HICO is actually operating. The predicted ISS orbit is used to program when to activate HICO and if the actual orbit differs slightly, at the time of data collection, the location of the targeted image might be off slightly. Images of the same area were acquired at different times of the day and at different solar zenith/azimuth and view zenith/azimuth angles due to the ISS orbit, which is not Sun-synchronous. ISS altitude adjustments resulted in changes in spatial resolution and coverage of the target area as scenes were collected at different altitudes owing to changes in the orbit of the ISS (i.e. predicted vs. actual orbit). We recognize that this problem was inherent with sensors flown on the low orbiting ISS. However, this may be beneficial when testing algorithm performance for geostationary satellites, since these satellites measure at different times of the day and under different viewing geometries in relation to the Sun. The ISS orbits the Earth 16 times per day, and HICO is currently limited to the acquisition of one image per orbit due to a combination of the time it takes HICO to complete an image and data downlink speeds from the ISS. In addition, during this study, several logistical conflicts with supply module dockings and general ISS operations led to rescheduling of planned image acquisitions and complications (e.g. logistical difficulties associated with scheduling field data collections at the time of an ISS overpass) because uncertain ISS ephemeris data beyond a two week time window made predicting the orbital path of the ISS (and image targeting) difficult more than two weeks into the future.

Additionally, HICO target overpass information was communicated only hours-to-days in advance based on a predictive model that incorporated ephemeris (orbit) and

predicted mean altitude parameters. Variations in ephemeris and oscillations in altitude made reliable estimates for ISS overpasses difficult. The uncertainty associated with overpass predictions negatively impacted the potential to effectively deploy field crews to implement sampling protocols in an efficient and timely manner.

Because satellite-based, hyperspectral data have been rarely available for scientific investigations, HICO has the potential to be a valuable monitoring tool owing to its high spectral and spatial resolutions and the corresponding ability to obtain spectral data near the land–water interface where water-quality managers continue to focus and humans may have the high probability of interacting with the aquatic environment. However, for HICO to transition from a proof-of-concept project to full application, the sensor needs to be placed into a polar orbit configuration to provide a stable well-characterized platform for greater spatial and temporal coverage and geometric fidelity. Furthermore, a polar orbiting platform would be highly predictable, allowing image synchronization with any field validation effort. This observation is consistent with the planning of NASA and other agencies to launch several ocean colour missions (e.g. GEO-CAPE, ACE, HyspIRI) with hyperspectral capacity in the future (NRC 2007).

Acknowledgements

This article has been subjected to review by the ORD National Health and Environmental Effects Research Laboratory and approved for publication. This is ORD Tracking Number ORD – 005315 and EPA Publication Number EPA/600/J13/173 of the Atlantic Ecology Division, National Health and Environmental Effects Research Laboratory, Office of Research and Development, US Environmental Protection Agency (EPA). Mention of trade names or commercial products does not constitute endorsement or recommendation for use. The views expressed in this article are those of the authors and do not necessarily reflect the views or policies of the US Environmental Protection Agency or the Naval Research Laboratory (NRL). We thank Robyn Conmy (EPA/National Risk Management Research Laboratory), Jessica Aukamp (EPA/NHEERL/Gulf Ecology Division (GED)), and George Craven (EPA/GED) for their support in planning and field operations. We also appreciate the assistance of Diane Yates (EPA/GED) for managing the database and providing quality assurance measures. James Hagy (EPA/GED), Michael Murrell (EPA/GED), Brandon Jarvis (EPA/GED), and Allyn Duffy (EPA/GED) provided support during field operations. David Lewis, Andrew Quaid, Courtney Kearney, and Sherwin Ladner (all at Naval Research Laboratory/Stennis Space Center) provided support with the HICO image processing and glider data collections. We also thank Bryan Milstead, Steve Rego, and Jeffrey Hollister at the EPA/NHEERL/Atlantic Ecology Division (EPA/AED) for their insightful review comments.

Funding

This work was funded by the US Environmental Protection Agency Office of Research and Development (ORD) under the Pathfinder Innovation Program and supported by the Safe and Sustainable Waters Research Program.

References

American Geological Institute. 1974. *Glossary of Geology*. Washington, DC: American Geological Institute.

Berk, A., G. P. Anderson, P. K. Acharya, J. H. Chetwynd, L. S. Bermstein, E. P. Shettel, M. W. Matthew, and S. M. Adler-Golden. 2000. *MODTRAN4 User's Manual*, 97. Hanscom AFB, MA: Air Force Research Laboratory, Space Vehicles Directorate, Air Force Material Command.

Binding, C. E., and D. G. Bowers. 2003. "Measuring the Salinity of the Clyde Sea From Remotely Sensed Ocean Colour." *Estuarine, Coastal and Shelf Science* 57: 605–611. doi:10.1016/S0272-7714(02)00399-2.

Bowers, D. G., D. Evans, D. N. Thomas, K. Ellis, and P. J. le B. Williams. 2004. "Interpreting the Colour of an Estuary." *Estuarine, Coastal and Shelf Science* 59: 13–20. doi:10.1016/j.ecss.2003.06.001.

Bowers, D. G., G. E. L. Harker, P. S. D. Smith, and P. Tett. 2000. "Optical Properties of a Region of Freshwater Influence (the Clyde Sea)." *Estuarine, Coastal and Shelf Science* 50: 717–726. doi:10.1006/ecss.1999.0600.

Cavalli, R. M., S. Pignatti, and E. Zappitelli. 2006. "Correction on Sun Glint Effect on MIVIS Data of the Sicily Campaign in July 2000." *Annals of Geophysics* 49: 277–286.

Chavez, P. S. 1988. "An Improved Dark-Object Subtraction Technique for Atmospheric Scattering Correction of Multispectral Data." *Remote Sensing of Environment* 24: 459–479. doi:10.1016/0034-4257(88)90019-3.

Chen, Z. 2006. "Monitoring Water Quality in Tampa Bay: Coupling *In Situ* and Remote Sensing." In *Graduate School Theses and Dissertations.* http://scholarcommons.usf.edu/etd/2479.

Chen, Z., C. Hu, and F. Muller-Karger. 2007. "Monitoring Turbidity in Tampa Bay Using MODIS/Aqua 250–M Imagery." *Remote Sensing of Environment* 109: 207–220. doi:10.1016/j.rse.2006.12.019.

Chen, Z., C. Hu, R. N. Conmy, F. Muller-Karger, and P. Swarzenski. 2007. "Colored Dissolved Organic Matter in Tampa Bay, Florida." *Marine Chemistry* 104: 98–109. doi:10.1016/j.marchem.2006.12.007.

Coble, P. G. 2007. "Marine Optical Biogeochemistry: The Chemistry of Ocean Color." *Chemical Reviews* 107: 402–418. doi:10.1021/cr050350+.

Corson, M. R. 2011. "The Hyperspectral Imager for the Coastal Ocean: Littoral Environmental Characterization From the International Space Station." Proceedings of ocean optics XX, Anchorage, AK, September 27–October 1.

Corson, M. R., and C. O. A. Davis. 2011. "A New View of Coastal Oceans From the Space Station." *Eos, Transactions American Geophysical Union* 92 (19): 161–162. doi:10.1029/2011EO190001.

Dall'Olmo, G., and A. Gitelson. 2006. "Effect of Bio-Optical Parameter and Uncertainties in Reflectance Measurements on the Remote Estimation of Chlorophyll-a Concentration in Turbid Productive Waters: Modeling Results." *Applied Optics* 45 (15): 3577–3592. doi:10.1364/AO.45.003577.

Dall'Olmo, G., A. Gitelson, and D. C. Rundquist. 2003. "Towards a Unified Approach for Remote Estimation of Chlorophyll-a in Both Terrestrial Vegetation and Turbid Productive Waters." *Geophysical Research Letters* 30: 1038.

Dall'Olmo, G., A. Gitelson, D. C. Rundquist, B. Leavitt, T. Barrow, and J. C. Holz. 2005. "Assessing the Potential of SeaWiFS and MODIS for Estimating Chlorophyll Concentrations in Turbid Productive Waters Using Red and Near-Infrared Bands." *Remote Sensing of Environment* 96 (2): 176–187. doi:10.1016/j.rse.2005.02.007.

Devlin, M., S. Bricker, and S. Painting. 2011. "Comparison of Five Methods for Assessing Impacts of Nutrient Enrichment Using Estuarine Case Studies." *Biogeochemistry* 106: 177–205. doi:10.1007/s10533-011-9588-9.

D'Sa, E. J., R. L. Miller, and C. E. Del Castillo. 2006. "An Assessment of Short-Term Physical Influences on the Bio-Optical Properties and Ocean Color Algorithms in Coastal Waters Influenced by the Mississippi River." Applied Optics 45 (28): 7410–7428. doi:10.1364/AO.45.007410.

ENVI. Atmospheric CorrectionModule. 2009. "QUAC and FLAASH User's Guide." In *Atmospheric Correction Module Version 4.7*, 43. Boulder, CO: ITT Visual Information Solutions.

Ferreira, J. G., J. H. Andersen, A. Borja, S. B. Bricker, J. Camp, M. C. D. Silva, E. Garcés, A.-S. Heiskanen, C. Humborg, L. Ignatiades, C. Lancelot, A. Menesguen, P. Tett, N. Hoepffner, and U. Claussen. 2011. "Overview of Eutrophication Indicators to Assess Environmental Status within the European Marine Strategy Framework Directive Estuaries." *Estuarine, Coastal and Shelf Science* 93: 117–131. doi:10.1016/j.ecss.2011.03.014.

Gitelson, A. 1992. "The Peak Near 700 nm on Radiance Spectra of Algae and Water-Relationships of its Magnitude and Position with Chlorophyll Concentration." *International Journal of Remote Sensing* 13: 3367–3373. doi:10.1080/01431169208904125.

Gitelson, A. A., B.-C. Gao, R.-R. Li, S. V. Berdnikov, and V. Saprygin. 2011. "Estimation of Chlorophyll-a Concentration In Productive Turbid Waters Using A Hyperpectral Imager For The Coastal Ocean-The Azov Sea Case Study." *Environmental Research Letters* 6: 024023. doi:10.1088/1748-9326/6/2/024023.

Gitelson, A. A., D. Gurlin, W. Moses, and T. Barrow. 2009. "A Bio-Optical Algorithm for the Remote Estimation of the Chlorophyll *a* Concentration in Case 2 Waters." *Environmental Research Letters* 14 (4): 5.

Gitelson, A. A., G. Dall'olmo, W. Moses, D. C. Rundquist, T. Barrow, T. R. Fisher, D. Gurlin, and J. Holz. 2008. "A Simple Semi-Analytical Model for Remote Estimation of Chlorophyll-a Concentraton in Turbid Productive Waters: Validation." *Remote Sensing of Environment* 112: 3582–3593. doi:10.1016/j.rse.2008.04.015.

Gitelson, A. A., J. F. Schalles, and C. M. Hladik. 2007. "Remote Chlorophyll-a Retrieval in Turbid Productive Estuaries: Chesapeake Bay Study." *Remote Sensing of Environment* 109: 464–472. doi:10.1016/j.rse.2007.01.016.

Goa, B. C., M. J. Montes, Z. Ahmad, and C. O. Davis. 2000. "Atmospheric Correction Algorithm for Hyperspectral Remote Sensing of Ocean Color From Space." *Applied Optics* 39: 887–896. doi:10.1364/AO.39.000887.

Gons, H., M. Auer, and S. Effler. 2008. "MERIS Satellite Chlorophyll Mapping of Oligotrophic and Eutrophic Waters in the Laurentian Great Lakes." *Remote Sensing of Environment* 112: 4098–4106.

Gons, H. J. 1999. "Optical Teledetection of Chlorophyll – *a* in Turbid Inland Waters." *Environmental Science and Technology* 33: 1127–1132. doi:10.1021/es9809657.

Goodman, J. A., Z. Lee, and S. L. Ustin. 2008. "Influence of Atmospheric and Sea-Surface Corrections on Retrieval of Bottom Depth and Reflectance Using a Semi-Analytical Model: A Case Study in Kaneohe Bay, Hawaii." *Applied Optics* 47: F1–F11. doi:10.1364/AO.47.0000F1.

Gordon, H. R., and A. Morel. 1983. "Remote Assessment of Ocean Color for Interpretation of Satellite Visible Imagery – A Review." In *Lecture Notes on Coastal and Estuarine Studies*, edited by R. T. Barber, N. K. Mooers, M. J. Bowman, and B. Zeitzschel, 114. New York, NY: Springer-Verlag.

Gordon, H. R., and M. Wang. 1994. "Retrieval of Water-Leaving Radiance and Aerosol Optical Thickness Over the Oceans with SeaWiFS: A Preliminary Algorithm." *Applied Optics* 33 (3): 443–452. doi:10.1364/AO.33.000443.

Gould, R. W., R. A. Arnone, and M. Sydor. 2001. "Absorption, Scattering, and Remote-Sensing Reflectance Relationships in Coastal Waters: Testing a New Inversion Algorithm." *Journal of Coastal Research* 17 (2): 328–341.

Gould Jr., R. W., R. A. Arnone, and P. M. Martinolich. 1999. "Spectral Dependence of the Scattering Coefficient in Case 1 and Case 2 Waters." *Applied Optics* 38 (12): 2377–2383. doi:10.1364/AO.38.002377.

Gower, J. F. R., R. Doerffer, and G. A. Borstad. 1999. "Interpretation of the 685 Nm Peak in Water-Leaving Radiance Spectra in Terms of Fluorescence, Absorption, and Scattering, and Its Observation by MERIS." *International Journal of Remote Sensing* 20: 1771–1786. doi:10.1080/014311699212470.

Themistocleous, K. C., D. J. Hadjimitsis, A. Retalis, and N. Chrysoulakis. 2012. "Development of an Image Based Atmospheric Correction Algorithm for Aerosol Optical Thickness Retrieval Using the Darkest Pixel Method." *Journal of Applied Remote Sensing* 6: 063538–12. doi:10.1117/1.JRS.6.063538.

Hansen, J. E., and L. Travis. 1974. "Light Scattering in Planetary Atmospheres." *Space Science Reviews* 16: 527–610. doi:10.1007/BF00168069.

Heyes, A., C. Miller, and R. Mason. 2004. "Mercury and Methylmercury in Hudson River Sediment: Impact of Tidal Resuspension on Partitioning and Methylation." *Marine Chemistry* 90 (1–4): 75–89.

Hochberg, E. J., S. Andrefouet, and M. R. Tyler. 2003. "Sea Surface Correction of High Spatial Resolution IKONOS Images to Improve Bottom Mapping in Near-Shore Environments." *IEEE Transactions on Geoscience and Remote Sensing* 41: 1724–1729. doi:10.1109/TGRS.2003.815408.

Hu, C., Z. Chen, T. D. Clayton, P. Swarzenski, J. C. Brock, and F. Muller–Karger. 2004. "Assessment of Estuarine Water-Quality Indicators Using MODIS Medium-Resolution Bands: Initial Results From Tampa Bay, FL." *Remote SenSing of Environment* 93: 423–441. doi:10.1016/j.rse.2004.08.007.

Hunter, P. D., A. N. Tyler, L. Carvalho, G. A. Codd, and S. C. Maberly. 2010. "Hyperspectral Remote Sensing of Cyanobacterial Pigments as Indicators for Cell Populations and Toxins in Eutrophic Lakes." *Remote Sensing of Environmen*t 114: 2705–2718. doi:10.1016/j.rse.2010.06.006.

Kay, S., J. D. Hedley, and S. Lavender. 2009. "Sun Glint Correction of High and Low Spatial Resolution Images of Aquatic Scenes: A Review of Methods for Visible and Near-Infrared Wavelengths." *Remote Sensing* 1: 697–730. doi:10.3390/rs1040697.

Keith, D. J., J. A. Yoder, and S. A. Freeman. 2002. "Spatial and Temporal Distribution of Coloured Dissolved Organic Matter (CDOM) in Narragansett Bay, Rhode Island: Implications for Phytoplankton in Coastal Waters." *Estuarine, Coastal and Shelf Science* 55: 705–717. doi:10.1006/ecss.2001.0922.

Ladner, S. D., J. C. Sandidge, P. E. Lyon, R. A. Arnone, R. W. Gould, Z. P. Lee, and P. M. Martinolich. 2007. "Development of Higher Resolution Optical Properties From MODIS." In *Proceedings of SPIE Coastal Ocean Remote* Sensing, edited by Robert J. Frouin, ZhongPing Lee, Vol. 6680, 668013-1-668013-9. doi:10.1117/12.736845.

Laws, E. 1997. *Chapter 4 – Model II Linear Regression. Mathematical Methods for Oceanographers*, 57–71. New York: John Wiley and Sons.

Le, C., C. Hu, J. P. Cannizzaro, D. English, F. Muller-Karger, and Z. Lee. 2013. "Evaluation of Chlorophyll-a Remote Sensing Algorithms for an Optically Complex Estuary." *Remote Sensing of Environment* 129: 75–89. doi:10.1016/j.rse.2012.11.001.

Le, C., Y. Li, Y. Zha, D. Sun, C. Huang, and H. Lu. 2009. "A Four-Band Semi-Analytical Model for Estimating Chlorophyll *a* in Highly Turbid Lakes: The Case of Taihu Lake, China." *Remote Sensing of Environment* 113: 1175–1182. doi:10.1016/j.rse.2009.02.005.

Le, C., Y. Zha, Y. Li, D. Sun, H. Lu, and B. Yin. 2010. "Eutrophication of Lake Waters in China: Cost, Causes, and Control." *Environmental Management* 45: 662–668.

Lewis, D., R. W. Gould Jr, A. Weidemann, S. Ladner, and Z. Lee. 2013. "Bathymetry Estimations Using Vicariously Calibrated HICO Data. Ocean Sensing and Monitoring V." In *Proceedings of SPIE*, edited by W. Hou and R. A. Arnone, Vol. 8724, 87240N-1–87240N-12. doi:10.1117/12.2017864.

Lucke, R. L., M. Corson, N. R. McGlothlin, S. D. Butcher, D. L. Wood, D. R. Korwan, R. R. Li, W. A. Snyder, C. O. Davis, and D. T. Chen. 2011. "Hyperspectral Imager for the Coastal Ocean: Instrument Description and First Images." *Applied Optics* 50 (11): 1501–1516. doi:10.1364/AO.50.001501.

Martinolich, P. M., and T. Scardino. 2011. *Automated Processing System User's Guide Version 4.2.* Washington, DC: NRL. http://www7333.nrlssc.navy.mil/docs/aps_v4.2/html/user/aps_chunk/index.xhtml.

Miller, R. L., and B. A. McKee. 2004. "Using MODIS Terra 250 M Imagery to Map Concentrations of Total Suspended Matter in Coastal Waters." *Remote Sensing of Environment* 93: 259–266. doi:10.1016/j.rse.2004.07.012.

Mobley, C. D. 1999. "Estimation of Remote-Sensing Reflectance From Above-Surface Measurements." *Applied Optics* 38: 7442–7455. doi:10.1364/AO.38.007442.

Morel, A., and L. Prieur. 1977. "Analysis of the Variations in Ocean Color." *Limnology Oceanography* 22: 709–722.

Moses, W. J., A. A. Gitelson, R. L. Perk, D. Gurlin, D. C. Rundquist, B. C. Leavitt, T. M. Barrow, and P. Brakhage. 2012. "Estimation of Chlorophyll-a Concentration in Turbid Productive Waters Using Airborne Hyperspectral Data." *Water Research* 46: 993–1004. doi:10.1016/j.watres.2011.11.068.

Moses, W. J., A. A. Gitelson, S. Berdnikov, and V. Povazhnyy. 2009. "Estimation of Chlorophyll-a Concentration in Case II Waters Using MODIS and MERIS Data-Successes and Challenges." *Environmental Research Letters* 4. doi:10.1088/1748-9326/4/4/045005.

National Research Council. 2007. "*Earth Science and Applications From Space: National Imperatives for the Next Decade and Beyond. Committee on Earth Science and Applications From Space: A Community Assessment and Strategy for the Future*", 456. Washington, DC: National Research Council 0-309-66714-3.

Nevers, M. B., and R. L. Whitman. 2005. "Nowcast Modeling of Escherichia Coli Concentrations at Multiple Urban Beaches of Southern Lake Michigan." *Water Research* 39: 5250–5260. doi:10.1016/j.watres.2005.10.012.

NIST/SEMATECH. 2012. *Chapter 7.1.6. What are Outliers in the Data? NIST/SEMATECH e-Handbook of Statistical Methods.* http://www.itl.nist.gov/div898handbook/April2012.

O'Reilly, J. E., S. Maritorena, B. G. Mitchell, D. A. Siegel, K. L. Carder, S. A. Garver, M. Kahru, and C. R. McClain. 1998. "Ocean Color Chlorophyll Algorithms for SeaWiFS." *Journal of Geophysical Research* 103 (C11): 24,937–24,953

Oregon State University – HICO. 2011. *Working with the Data – Geolocating the Data.* http://hico.coas.oregonstate.edu/datsets/geolocation.shtml.

Palandro, D. A. 2006. "Coral Reef Habitat Change and Water Clarity Assessment (1984–2002) for the Florida Keys National Marine Sanctuary Using Landsat Satellite Data." Dissertation, 116. University of South Florida, Tampa.

Pegau, S., J. V. R. Zaneveld, B. Mitchell, G. Mueller, J. L. Kahru, M. Wieland, J. Malgorzat, and M. Stramska. 2003. *Inherent Optical Properties: Instruments, Characterizations, Field Measurements and Data Analysis Protocols*, NASA/TM-2003-211621/Rev4 - Vol. IV. Greenbelt, MD: Goddard Space Flight Center.

Ricker, M. C., B. K. Odhiambo, and J. M. Church. "Spatial Analysis of Soil Erosion and Sediment Fluxes: A Paired Watershed Study of Two Rappahannock River Tributaries, Stafford County, Virginia." *Environmental Management* 41 (5): 766–778. doi:10.1007/s00267-008-9094-6.

Schaeffer, B. A., J. D. Hagy, J. C. Lehrter, R. N. Conmy, and R. Stumpf. 2012. "An Approach to Developing Numeric Water Quality Criteria for Coastal Waters Using the SeaWiFS Satellite Data Record." *Environmental Science and Technology* 46: 916–922. doi:10.1021/es2014105.

Schaeffer, B. A. 2011. "HICO – Pathfinder Innovation Project: Quality Assurance Project Plan." EPA QAPP-GED/EDEB/BS/2011-01-001, 31 May 2011.

Stumpf, R. P., M. E. Culver, P. A. Tester, M. Tomlinson, G. J. Kirkpatrick, B. A. Pederson, E. Truby, V. Ransibrahmanakul, and M. Soracco. 2003. "Monitoring Karenia Brevis Blooms in the Gulf of Mexico Using Satellite Ocean Color Imagery and Other Data." *Harmful Algae* 2: 147–160. doi:10.1016/S1568-9883(02)00083-5.

Tehrani, N. C., E. J. D'Sa, C. Osburn, T. S. Bianchi, and B. A. Schaeffer. 2013. "Chromophoric Dissolved Organic Matter and Dissolved Organic Carbon From SeaWiFS, MODIS and MERIS Sensors: Case Study for the Northern Gulf of Mexico." *Remote Sensing* 5: 1439–1464. doi:10.3390/rs5031439.

Tiwari, S. P., and P. Shanmugam. 2011. "An Optical Model for the Remote Sensing of Coloured Dissolved Organic Matter in Coastal/Ocean Waters." *Estuarine, Coastal and Shelf Science* 93: 396–402. doi:10.1016/j.ecss.2011.05.010.

Tufillaro, N., C. O. Davis, and K. B. Jones. 2011. "Indicators of Plume Constituents From HICO." Proceedings of ocean optics XX, Anchorage, AK, September 27–October 1.

Van Stokkom, H. T. C. and R. Guzzi. 1984. "Atmospheric Spectral Attenuation of Airborne Remote Sensing Data: Comparison Between Experimental and Theoretical Approaches." *International Journal of Remote Sensing* 5: 925–938.

Wang, H., C. M. Hladik, W. Huang, K. Milla, L. Edmiston, M. A. Harwell, and J. F. Schalles. 2010. "Detecting the Spatial and Temporal Variability of Chlorophyll-a Concentration and Total Suspended Solids in Apalachiocola Bay, Florida Using MODIS Imagery." *International Journal of Remote Sensing*: 439–453. doi:10.1080/01431160902893485.

Welschmeyer, N. A. 1994. "Fluorometric Analysis of Chlorophyll a in the Presences of Chlorophyll b and Phaeopigments." *Limnology and Oceanography* 39: 1985–1992. doi:10.4319/lo.1994.39.8.1985.

Werdell, P. J., S. W. Bailey, B. A. Franz, L. W. Harding, Jr., G. C. Feldman, and C. R. McClain. 2009. "Regional and Seasonal Variability of Chlorophyll-a in Chesapeake Bay as Observed by SeaWiFS and MODIS-Aqua." *Remote Sensing of Environment* 113: 1319–1330.

Witter, D. L., J. D. Ortiz, S. Palm, R. T. Heath, and J. W. Budd. 2009. "Assessing the Application of SeaWiFS Ocean Color Algorithms to Lake Erie." *Journal of Great Lakes Research* 35 (3): 361–370.

Zhang, Y., Y. Yin, L. Feng, G. Zhu, Z. Shi, X. Liu, and Y. Zhang. 2011. "Characterizing Chromophoric Dissolved Organic Matter in Lake Tianmuhu and Its Catchment Basin Using Excitation-Emission Matrix Fluorescence and Parallel Factor Analysis." *Water Research* 45 (16): 5110–5122. doi:10.1016/j.watres.2011.07.014.